THE OHIO STATE UNIVERSITY

Electromagnetic On-Aircraft Antenna Radiation in the Presence of Composite Plates

S.H-T. Kan and R.G. Rojas

The Ohio State University

ElectroScience Laboratory

Department of Electrical Engineering
Columbus, Ohio 43212

Technical Report 722792-5
Grant No. NAG-1-1058
July 1994

National Aeronautics and Space Administration
Langley Research Center
Hampton, VA 23665-5225

NOTICES

When Government drawings, specifications, or other data are used for any purpose other than in connection with a definitely related Government procurement operation, the United States Government thereby incurs no responsibility nor any obligation whatsoever, and the fact that the Government may have formulated, furnished, or in any way supplied the said drawings, specifications, or other data, is not to be regarded by implication or otherwise as in any manner licensing the holder or any other person or corporation, or conveying any rights or permission to manufacture, use, or sell any patented invention that may in any way be related thereto.

50272-101

REPORT DOCUMENTATION PAGE	1. REPORT NO.	2.	3. Recipient's Accession No.

4. Title and Subtitle
Electromagnetic On-Aircraft Antenna Radiation in the Presence of Composite Plates

5. Report Date
July 1994

6.

7. Author(s)
S.H-T. Kan and R.G. Rojas

8. Performing Org. Rept. No.
722792-5

9. Performing Organization Name and Address
The Ohio State University
ElectroScience Laboratory
1320 Kinnear Road
Columbus, OH 43212

10. Project/Task/Work Unit No.

11. Contract(C) or Grant(G) No.
(C)
(G) NAG-1-1058

12. Sponsoring Organization Name and Address
National Aeronautics and Space Administration
Langley Research Center
Hampton, VA 23665

13. Report Type/Period Covered
Technical Report

14.

15. Supplementary Notes

16. Abstract (Limit: 200 words)

The UTD-based NEWAIR3 Code is modified such that it can model modern aircraft by composite plates. One good model of conductor-backed composites is the impedance boundary condition where the composites are replaced by surfaces with complex impedances. This impedance-plate model is then used to model the composite plates in the NEWAIR3 Code. In most application, the aircraft distorts the desired radiation pattern of the antenna. However, test examples conducted in this report have shown that the undesired scattered fields are minimized if the right impedance values are chosen for the surface impedance plates.

17. Document Analysis a. Descriptors

b. Identifiers/Open-Ended Terms

c. COSATI Field/Group

18. Availability Statement
A. Approved for public release;
Distribution is unlimited.

19. Security Class (This Report)
Unclassified

20. Security Class (This Page)
Unclassified

21. No. of Pages
82

22. Price

(See ANSI-Z39.18) *See Instructions on Reverse* OPTIONAL FORM 272 (4-77)
Department of Commerce

Contents

List of Figures

List of Tables

Chapter 1

Introduction

In recent years, practical applications related to the scattering of electromagnetic waves by objects that are not perfectly conducting have gained significant attention. One very important application of this type of electromagnetic scattering is the study of antennas mounted on aircraft. Composite materials are being used more frequently in the construction of modern aircraft, and their electromagnetic properties are such that they cannot be modeled by perfect electrical conductors (PECs) as was done in the past to model good conductors such as aluminum. Several computer codes have been developed in the last few years to study the radiation properties of antennas mounted on complex structures. One example of this type of code is the NEWAIR3 Code [1, 2] developed at the ElectroScience Laboratory of The Ohio State University. This code is based on the Uniform Theory of Diffraction (UTD) [3, 4, 5] and is used to study antennas mounted on the fuselage of aircraft. This code uses an ellipsoid [1, 2, 6, 7] to model the fuselage of the aircraft and flat plates to model the rest of the aircraft. It is assumed that the ellipsoid and plates are PECs which as mentioned before is a good model for good conductors. Thus, the NEWAIR3 Code needs to be modified to be able to model modern aircraft constructed from composite materials. One good model of conductor-backed composites is the impedance boundary condition [8] where the composites are replaced by surfaces with complex impedances. These impedances are complex, and thus the composites may be lossy.

The first step in the process of modifying the UTD-based NEWAIR3 is to add the capability of modeling composite flat plates by impedance plates. The second,

and more difficult step, is to replace the PEC ellipsoid by an ellipsoid whose surface can be modeled by a complex impedance. This second step is not the subject of this report, but it is being pursued at the ElectroScience Laboratory. The following will briefly describe the original NEWAIR3 Code and also briefly review the literature concerning the electromagnetic diffraction by a wedge with impedance faces.

1.1 Brief Literature Overview

The NEWAIR3 Code is a Fortran computer code developed at the Ohio State University to investigate the radiation patterns of antennas which are mounted on an aircraft fuselage. The fuselage is modeled by a composite ellipsoid, and other parts of the aircraft are modeled by a number of flat plates. Note that the term "composite ellipsoid" simply means that two ellipsoids are joined at the antenna location and does not refer to its electrical properties. This "composite ellipsoid" and the flat plates are assumed to be PECs. By providing an input data file described by the Airborne Antenna Radiation Pattern (AARP) User's Manual [1], the far-zone and near-zone radiation patterns are computed based on the UTD [3, 4, 5].

In order to modify the NEWAIR3 Code to have surface impedance plates, the literature related to the fields scattered by impedance wedges was studied. There are basically two methods to solve for the fields scattered by impedance wedges, namely, the Wiener-Hopf and the Maliuzhinets methods. The method developed by Maliuzhinets [9] is suitable for studying wedge-shaped objects. In 1988, Rojas [10] obtained an UTD solution based on the generalized reflection method, which is more general than the Weiner-Hopf method [11]. This paper provides an uniform asymptotic solution for the electromagnetic diffraction by an impedance wedge for four special wedge angles. These four wedge angles are 0 (half-plane), $\pi/2$ (right-angled interior wedge), π (two-part plane), and $3\pi/2$ (right-angled exterior wedge). The incident field to these wedges is assumed to be an arbitrary polarized plane wave which is obliquely incident to the axis of the wedge. The solution in [10] is written in a compact matrix notation which is very suitable for numerical computations, and it will be used to calculate the diffracted fields from impedance wedges.

1.2 Report Organization

In Chapter 2, the solutions for the geometrical optics fields, which include the source and reflected fields, will be discussed. The first section will summarize the source-field solutions for monopole antennas and aperture-typed antennas, which include axial slots, circumferential slots, and rectangular microstrip patch antennas. The solutions for monopoles and slots are described in Kim's dissertation [2], and the microstrip antenna results are obtained from Rojas and Ly [12]. Following the source-field solutions, a new Fresnel reflection coefficient, for which the total field (incident plus reflected) satisfies the impedance boundary condition at the surface of the plate, is derived. The incident field is assumed to be an arbitrary polarized plane wave. This solution is then modified to compute the reflected fields in the NEWAIR3 Code, and is latter applied to obtain the solution for multiple reflected fields. For all field components in this chapter, an $e^{j\omega t}$ time dependence is assumed and suppressed from all the mathematical expressions.

Chapter 3 documents the solutions for edge-diffracted fields for an arbitrary-polarized plane wave incident upon an impedance wedge. The four special wedge angles considered here include 0, π, $1/2\pi$, and $3/2\pi$. These solutions are based on Rojas' solutions in [10]. In order to implement the solutions in the NEWAIR3 Code, modifications of some parameters are necessary and will be discussed in the last section of this chapter. For all field expressions in this chapter, an $e^{-i\omega t}$ time dependence is assumed and suppressed. As a result, it is necessary to take the complex conjugate of the diffracted-field solutions presented in this chapter before the solutions can be implemented in the NEWAIR3 Code.

Chapter 4 will present numerical results for the impedance plates. This chapter will first show numerical results for various plane-wave incident cases, and then various ellipsoid-plate models will be simulated with the NEWAIR3 Code. The first section will emphasize on the reflected and diffracted fields with a plane wave as the incident field. To illustrate the field behavior for various surface impedance values, field amplitudes for both the reflected and diffracted fields will be plotted as func-

tions of the surface impedance. Following these examples, the diffracted field as a function of the observation angles will also be investigated. The next section will discuss the results obtained with the modified NEWAIR3 Code. Seven examples including three ellipsoid-plate geometries are investigated. For the purpose of assessing the validity of the diffraction solutions discussed in Chapter 3, the first example will show the individual field component and the approximated first-order total field. In most applications, the aircraft distorts the desired radiation pattern of the antenna. Thus, the examples here will mainly show that the undesired reflected and diffracted fields can be minimized by choosing the right surface impedance value for the plates. The simulation results for the impedance plates are compared to the ones for the PEC plates. Each model considered in the NEWAIR3 Code section will have a PEC fuselage and a number of flat impedance plates.

The final chapter, Chapter 5, summarizes the study conducted for this report. A brief description on the future work related to the current study is also included at the end of this chapter.

Two appendices are provided following Chapter 5. The first appendix documents all modifications and additions to the NEWAIR3 Code. Some mathematical details and expressions involving the diffraction solutions discussed in Chapter 3 are documented and summarized in Appendix B.

Chapter 2

Geometrical-Optics Fields from Impedance Wedges

This chapter will discuss the geometrical-optics (GO) fields, which are a part of the high-frequency solution for our aircraft radiation problems. As mentioned before, the fuselage of the aircraft is modeled by a perfectly electrical conducting (PEC) composite ellipsoid [1] in the vicinity of the antenna. The rest of the aircraft body is modeled by flat plates that can have PEC or impedance surfaces.

In this analysis, it is assumed that the source and observation points are far enough from any impedance surfaces and impedance edges, and that the impedance surfaces are lossy enough so the contribution from surface ray fields can be neglected. The total electric field $\bar{E}^{total}$ for the on-aircraft antenna radiation can then be expressed as

$$\bar{E}^{total} = \bar{E}^{GO} + \bar{E}^{d} + \bar{E}^{cw} + \text{higher order terms}, \tag{2.1}$$

where $\bar{E}^{GO}$ are the GO fields, $\bar{E}^{d}$ are the edge-diffracted fields, and $\bar{E}^{cw}$ are the corner diffracted fields. Higher order terms would include multiple reflected, diffracted, reflected-diffracted fields, etc. For most calculations, the first three terms in Equation (2.1) are sufficient; however, there are situations where some higher order terms are needed. The lack of higher order terms is usually observed when the radiation pattern has jumps or discontinuities in its first derivative. The corner diffracted field for an impedance plate has not yet been obtained and it will be the subject of further research.

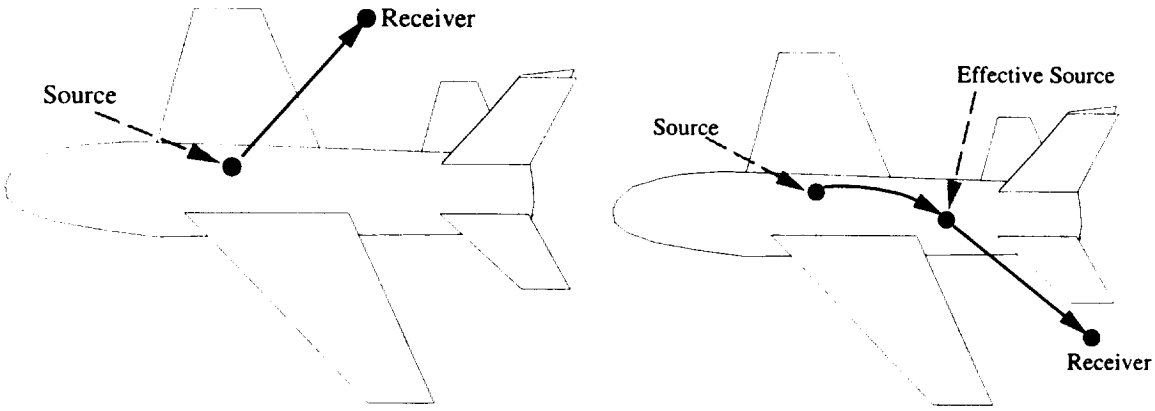

(a) Direct Source Field (b) Curved-Surface Diffracted Field

Figure 2.1: Geometry of an aircraft model for direct-source field (a) and curved-surface diffracted field (b), both fields are referred to as source fields.

For the aircraft models considered in this report, the geometrical-optics field $\tilde{E}^{GO}$ is composed of the total source field $\tilde{E}^{s}_{total}$ and the total reflected field $\tilde{E}^{r}_{total}$. The total source field consists of the direct electric field from a given source (i.e., the direct source field) when the observation point is in the lit region or the surface diffracted source field when the observation point is in the shadow region. The boundary between the lit and shadow region is a plane tangent to the curved surface at the antenna location.

Although the addition of impedance plates does not affect the source-field calculation in the NEWAIR3 Code, the expressions used for these fields are summarized in the next section.

2.1 Source Field with Antenna Mounted On a Convex Surface

The source is assumed to be mounted on the aircraft fuselage which is a convex surface modeled by a composite ellipsoid. The source shown in Figure 2.1 can be a monopole, a slot, or a microstrip patch antenna. For the monopole source, the current density is assumed to be a sinusoidal distribution with an unit amplitude over the monopole with length L. There are two different types of slot antennas

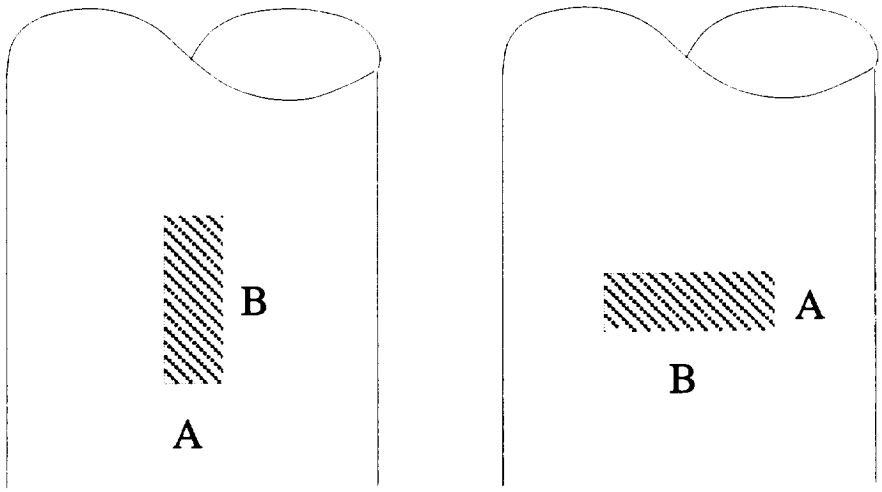

(a) Axial Slot (b) Circumferential Slot

Figure 2.2: A conducting cylinder upon which (a) an axial slot or (b) a circumferential slot is mounted.

available in the NEWAIR3 Code: (i) axial slots, and (ii) circumferential slots, as shown in Figures 2.2(a) and (b). Recently, a third antenna type has been added to the NEWAIR3 Code, namely, a rectangular microstrip patch. This patch is modeled by the well known cavity model as shown in Figure 2.3 where two magnetic current sources are placed along the radiating edges to calculate the radiated field of the dominant mode. Since the aircraft code already models slot antennas [1, 2] with magnetic dipoles, the fields radiated by these two magnetic current sources can be calculated; however, in the aircraft code, a slot is assumed to have a cosine field distribution along its long dimension. To model the microstrip patch antenna, it is assumed that the currents along the length of the dipoles are constant. Thus, the existing NEWAIR3 Code is modified so that a constant field distribution along the slot's long dimension can also be modeled. For more information about the modified code or the microstrip patch antenna, please refer to [13] and Appendix A.

As discussed in [2], the source field can be expressed in terms of the pattern factors: $\bar{P}_e$ and $\bar{P}_m$. These pattern factors are related to the dimensions of the sources, including the length of a monopole L and the dimensions A and B of a slot or a microstrip patch antenna. By referring to Section II-B.3 in [2] and [12], the

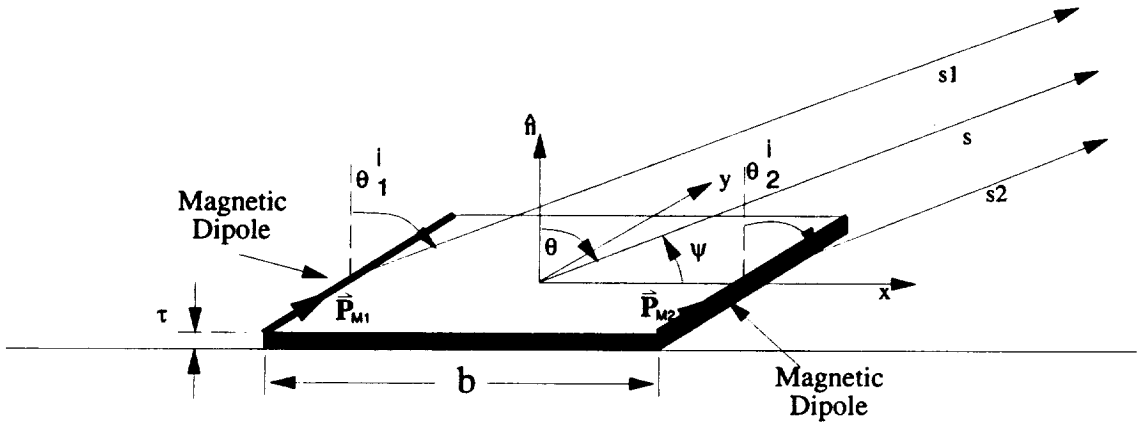

Figure 2.3: The cavity model for a rectangular microstrip patch antenna operating near the lowest-order resonant frequency f_{10} with a far-zone field location.

pattern factors $\bar{P}_e$ and $\bar{P}_m$ for field points in the lit or shadow region are given by the following expressions:

(i) the receiver in the shadow region:

For slot (or magnetic current dipoles) with a cosine field distribution along long dimension,

$$\bar{P}_m = \hat{P}_m \frac{2B}{\pi} \left[\frac{\cos(\frac{kB}{2}(\hat{P}_m \cdot \hat{t}'))}{1 - (\frac{kB}{\pi}(\hat{P}_m \cdot \hat{t}'))^2} \right] \left[\frac{\sin(\frac{kA}{2}(\hat{P}_m \cdot \hat{b}'))}{\frac{kA}{2}(\hat{P}_m \cdot \hat{b}')} \right]. \tag{2.2}$$

For electric current monopoles,

$$\bar{P}_e = \hat{n}'[1 - \cos(kL)]. \tag{2.3}$$

For slot (or magnetic current dipoles) with a constant field distribution along long dimension,

$$\bar{P}_{mj} = \hat{P}_{m_j} \left[\frac{C_0 \tau A \sin(\frac{k\tau}{2} \cos(\theta_j^i))}{\frac{k\tau}{2} \cos(\theta)_j^i} \right] \left[\frac{\sin(\frac{hA}{2} \sin(\theta_j^i)(\hat{P}_{m_j} \cdot \hat{t}'_j))}{\frac{hA}{2} \sin(\theta_j^i)(\hat{P}_{m_j} \cdot \hat{t}'_j)} \right]; \quad j = 1, 2 \tag{2.4}$$

where $\theta_j^i = 90^o$ in the above equation and C_0 is the constant that depends on the type of feed used to excite the antenna.

(ii) the receiver in the lit region:

For slot (or magnetic current dipoles) with a cosine field distribution along long

dimension,

$$\bar{P}_m = \hat{P}_m \frac{2B}{\pi} \left[\frac{\cos(\frac{kB}{2}\sin(\theta_i)(\hat{P}_m \cdot \hat{t}'))}{1-(\frac{kB}{\pi}\sin(\theta_i)(\hat{P}_m \cdot \hat{t}'))^2} \right] \left[\frac{\sin(\frac{kA}{2}\sin(\theta_i)(\hat{P}_m \cdot \hat{b}'))}{\frac{kA}{2}\sin(\theta_i)(\hat{P}_m \cdot \hat{b}')} \right]. \quad (2.5)$$

For electric current monopoles,

$$\bar{P}_e = \hat{n}' \frac{\cos(kL\hat{n}' \cdot \hat{s}) - \cos(kL)}{1-(\hat{n}' \cdot \hat{s})^2}. \quad (2.6)$$

For slot (or magnetic current dipoles) with a constant field along long dimension,

$$\bar{P}_{m_j} = \hat{P}_{m_j} \left[\frac{C_0 \tau A \sin(\frac{k\tau}{2}\cos(\theta_j^i))}{\frac{k\tau}{2}\cos(\theta)_j^i} \right] \left[\frac{\sin(\frac{hA}{2}\sin(\theta_j^i)(\hat{P}_{m_j} \cdot \hat{t'}_j))}{\frac{hA}{2}\sin(\theta_j^i)(\hat{P}_{m_j} \cdot \hat{t'}_j)} \right]; \quad j = 1,2. \quad (2.7)$$

Thus, the source-field solutions, which are expressed in terms of the pattern factors described above, are then summarized as follows for various antenna sources. Note that the source-field expressions of a rectangular microstrip patch antenna are based on the work of Rojas and Ly in [12].

(i) for a rectangular microstrip patch antenna with the receiver in the lit region [12],

$$\bar{E}_m^l = \begin{cases} \bar{L}_m^f & \text{in the far field} \\ \bar{L}_m^n \frac{e^{-jks}}{s} & \text{in the near field} \end{cases}, \quad (2.8)$$

where $\bar{L}_m^f$ can be written as

$$\bar{L}_m^f = 2\bar{P}_{m_0} \cos(\frac{kB}{2}(\hat{P}_{m_0} \cdot \hat{b}')\sin(\theta^i)), \quad (2.9)$$

where $\bar{P}_{m_0}$ is the same as $\bar{P}_{m_j}$ defined above, but it is located at the center of the patch. The angle θ^i is measured from the normal $\hat{n}$ of the microstrip to the field location as shown in Figure 2.3. The length B is approximately one half of the wavelength inside the substrate. In the near zone, $\bar{L}_m^n$ is the summation of two constant-current magnetic dipoles separated by a distance B. $\bar{L}_m^n$ for the receiver in the near-zone area is given as

$$\begin{aligned} \bar{L}_m^n &= 2\bar{P}_{m_0} \cos\left\{ \frac{kB}{2}\sin(\theta^i)(\hat{P}_{m_0} \cdot \hat{b}') \left[1 + \frac{B^2}{8s^2}\sin^2(\theta^i)(\hat{P}_{m_0} \cdot \hat{b}')^2 \right] \right\} \\ &\quad \cdot \exp\left[-jk \left\{ \frac{B^2}{8s^2}(1 - \sin^2(\theta^i)(\hat{P}_{m_0} \cdot \hat{b}')^2) \right. \right. \end{aligned}$$

$$-\frac{B^4}{128s^3}(1+\sin^4(\theta^i)(\hat{P}_{m_0}\cdot\hat{b}')^4)\Big\}\Big], \tag{2.10}$$

where the distance s is from the center of the microstrip to the field location as depicted in Figure 2.3. The angle ψ is measured from the x axis to the field direction of $\hat{s}$.

(ii) for a slot antenna with the receiver in the lit region,

$$\bar{E}_m^l = (L_m^n\hat{n} + L_m^b\hat{b})\begin{cases} \frac{e^{-jks}}{s} & \text{in the near field} \\ e^{jk\vec{P}_s\cdot\hat{P}_r} & \text{in the far field} \end{cases}, \tag{2.11}$$

where

$$\begin{aligned} L_m^n &= \frac{-jk}{4\pi}[(\bar{P}_m\cdot\hat{b}')(H^l + T_o^2F\cos(\theta^i)) + (\bar{P}_m\cdot\hat{t}')T_oF\cos(\theta^i)], \\ &\text{and} \\ L_m^b &= \frac{-jk}{4\pi}[(\bar{P}_m\cdot\hat{b}')T_oF + (\bar{P}_m\cdot\hat{t}')(S^l + T_o^2F\cos^2(\theta^i))]. \end{aligned} \tag{2.12}$$

(iii) for a monopole antenna with the receiver in the lit region,

$$\bar{E}_e^l = (L_e^n\hat{n} + L_e^b\hat{b})\begin{cases} \frac{e^{-jks}}{s} & \text{in the near field} \\ e^{jk\vec{P}_s\cdot\hat{P}_r} & \text{in the far field} \end{cases}, \tag{2.13}$$

where

$$\begin{aligned} L_e^n &= \frac{-jk\eta_0}{4\pi}\bar{P}_e\sin(\theta^i)[H^l + T_o^2F\cos(\theta^i)], \\ &\text{and} \\ L_e^b &= \frac{-jk\eta_0}{4\pi}\bar{P}_e\sin(\theta^i)T_oF.. \end{aligned} \tag{2.14}$$

All parameters and unit vectors used in the slot and monopole cases are discussed and documented in [2].

(iv) for a rectangular microstrip patch antenna with the receiver in the shadow region [12],

$$\bar{E}_m^s = \begin{cases} \bar{L}_m^n(\theta^i = 90^o)\frac{e^{-jks}}{\sqrt{s(\rho_c+s)}} & \text{in the near field} \\ \bar{L}_m^f(\theta^i = 90^o) & \text{in the far field} \end{cases}, \tag{2.15}$$

where $\bar{L}_m^n$ and $\bar{L}_m^f$ have the expressions given in Equation (2.10) and (2.9).

(v) for a slot antenna with the receiver in the shadow region,

$$\bar{E}_m^s = (D_m^n \hat{n} + D_m^b \hat{b}) \begin{cases} \frac{e^{-jks}}{\sqrt{s(\rho_c+s)}} & \text{in the near field} \\ e^{jk\vec{P}_{es}\cdot\hat{P}_r} & \text{in the far field} \end{cases}, \tag{2.16}$$

where

$$\begin{aligned} D_m^n &= \frac{-jk}{4\pi}(\bar{P}_m \cdot \hat{b}')He^{-jkt}\left[\frac{\rho_g(Q')}{\rho_g(Q)}\right]^{\frac{-1}{6}}, \\ &\text{and} \\ D_m^b &= \frac{-jk}{4\pi}\left[(\bar{P}_m \cdot \hat{b}')T_oS + (\bar{P}_m \cdot \hat{t}')S\right]e^{-jkt}\left[\frac{\rho_g(Q')}{\rho_g(Q)}\right]^{\frac{-1}{6}}. \end{aligned} \tag{2.17}$$

(vi) for a monopole antenna with the receiver in the shadow region,

$$\bar{E}_e^s = (D_e^n \hat{n} + D_e^b \hat{b}) \begin{cases} \frac{e^{-jks}}{\sqrt{s(\rho_c+s)}} & \text{in the near field} \\ e^{jk\vec{P}_{es}\cdot\hat{P}_r} & \text{in the far field} \end{cases}, \tag{2.18}$$

where

$$\begin{aligned} D_m^n &= \frac{-jk\eta_0}{4\pi}\bar{P}_e He^{-jkt}\left[\frac{\rho_g(Q')}{\rho_g(Q)}\right]^{\frac{-1}{6}}, \\ &\text{and} \\ D_m^b &= \frac{-jk\eta 0}{4\pi}\bar{P}_e T_o S e^{-jkt}\left[\frac{\rho_g(Q')}{\rho_g(Q)}\right]^{\frac{-1}{6}}. \end{aligned} \tag{2.19}$$

The parameters H, S, T_o, and all the unit vectors are discussed and defined in [2]. This section then summarized the source-field solution for the on-fuselage antenna radiations. This source field will be used as an incident field for computing single-reflected field in the aircraft code. The following section will derive the reflection coefficient for the plane-wave incident case and transform the solution to the NEWAIR3 Code.

2.2 Calculation of Reflected Field from Flat Impedance Surfaces

The NEWAIR3 Code already calculates high-frequency fields reflected from flat PEC surfaces as shown in Figure 2.4. The only modification that is needed to calculate

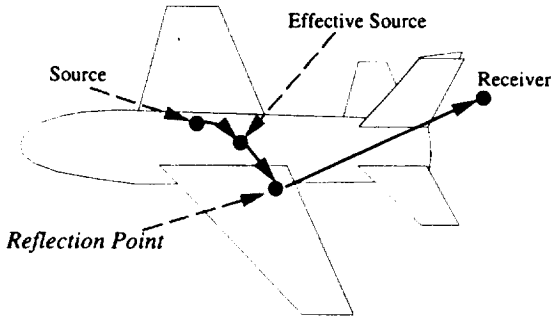

Figure 2.4: Geometry of an aircraft model for single-reflected fields.

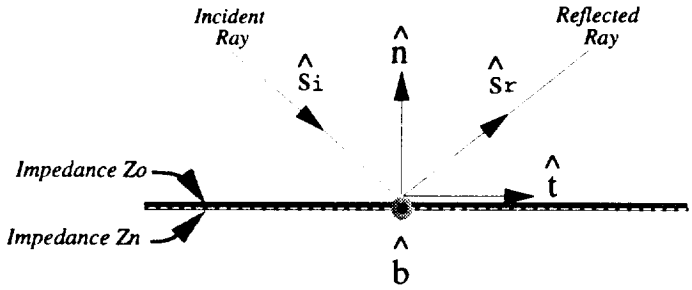

Figure 2.5: Surface-fixed coordinate system with incident field upon a plate with impedance faces.

reflected fields from impedance surfaces is the development of new dyadic Fresnel reflection coefficients in a ray-fixed coordinate system. It will be shown that the dyadic reflection coefficient for an impedance surface is very simple if ray-fixed coordinates are used.

To develop this Fresnel reflection coefficient, let us assume that a high-frequency field is incident on a flat surface with the surface impedance Z_0 on it as depicted in Figure 2.5. Since the field is assumed to be a high-frequency field, it follows that

$$\vec{H} \sim \frac{\hat{s} \times \vec{E}}{\eta_0}, \tag{2.20}$$

where $\hat{s}$ is the direction of propagation. Imposing the boundary condition at the surface of the plate, yields

$$\hat{n} \times \hat{n} \times \bar{E}^{total} = -Z_0 \hat{n} \times \bar{H}^{total},$$

or

$$\bar{E}^{total} - \hat{n}(\hat{n} \cdot \bar{E}^{total}) = Z_0 \hat{n} \times \bar{H}^{total}, \tag{2.21}$$

where $\hat{n}$ is the outward normal unit vector with respect to the given impedance surface, Z_0 is the surface impedance facing in the $\hat{n}$ direction, and $\bar{E}^{total}$, $\bar{H}^{total}$ are the total electric and magnetic fields at the boundary surface, respectively.

The coordinate system is first chosen to be the surface-fixed system (see Figure 2.5), in which three unit vectors with respect to the impedance plate are defined as a tangential unit vector $\hat{t}$, a normal unit vector $\hat{n}$, and a binormal unit vector $\hat{b} = \hat{t} \times \hat{n}$. The electric fields which are incident and reflected by the surface S can then be expressed in terms of these three unit vectors,

$$\bar{E}^{i,r} = \hat{t}E_t^{i,r} + \hat{n}E_n^{i,r} + \hat{b}E_b^{i,r}. \tag{2.22}$$

Choosing the reflection point Q_R to be the phase-reference point, it follows from Equation (2.21) and (2.20)that

$$\bar{E}^{total}(Q_R) - \hat{n}(E_n^i(Q_R) + E_n^r(Q_R)) = \frac{Z_0}{\eta_o} \cdot [(E_n^i(Q_R))\hat{s}^i - (\hat{n} \cdot \hat{s}^i)\bar{E}^i(Q_R) + (E_n^r(Q_R))\hat{s}^r - (\hat{n} \cdot \hat{s}^r)\bar{E}^r(Q_R)], \tag{2.23}$$

where $\bar{E}^i(Q_R)$ and $\bar{E}^r(Q_R)$ are the incident and reflected electric field at Q_R, respectively. $\bar{E}^{total}(Q_R)$ is the total field at the reflection point and $E_n^i(Q_R)$ and $E_n^r(Q_R)$ are the normal field components of $\bar{E}^i(Q_R)$ and $\bar{E}^r(Q_R)$, respectively. If all vector fields (i.e., $\bar{E}^i(Q_R)$, $\bar{E}^r(Q_R)$, and $\bar{E}^{total}(Q_R)$) are expressed in terms of unit vectors $\hat{t}$, $\hat{n}$, and $\hat{b}$ as in (2.22), then the reflection coefficient for the electric-field component perpendicular to the plane of incidence can be obtained by collecting terms in the binormal direction (i.e., the $\hat{b}$ component) on both sides of Equation (2.23):

$$E_b^r(Q_R) = E_b^i(Q_R)\left[\frac{-\frac{\eta_o}{Z_0} + \cos(\theta^i)}{\frac{\eta_o}{Z_0} + \cos(\theta^i)}\right], \tag{2.24}$$

where $\cos(\theta^i) = -\hat{n} \cdot \hat{s}^i$.

Next, the reflection coefficient for the electric-field component in the plane of incidence will be found. First, the incident and reflected ray-path directions (i.e., $\hat{s}^i$ and $\hat{s}^r$) can be decomposed into $\hat{n}$ and $\hat{t}$ unit coordinate pairs (see Figure 2.5):

$$\hat{s}^i = \hat{n}(\hat{s}^i \cdot \hat{n}) + \hat{t}(\hat{s}^i \cdot \hat{t}),$$

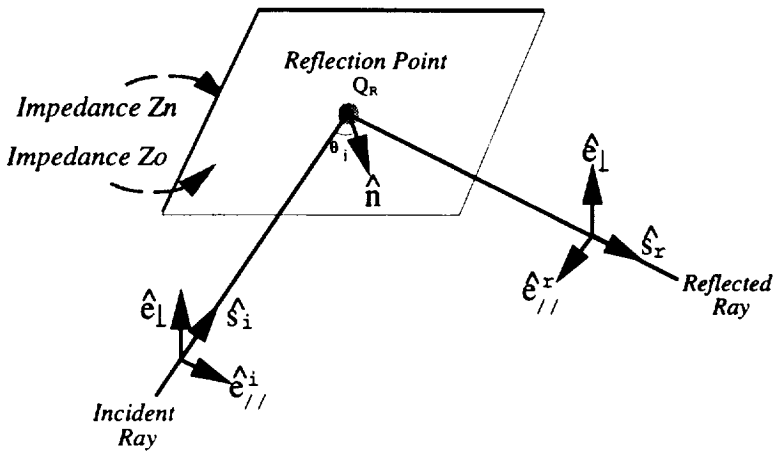

Figure 2.6: Ray-fixed coordinate system with field incident upon a plate with impedance faces.

and

$$\hat{s}^r = -\hat{n}(\hat{s}^i \cdot \hat{n}) + \hat{t}(\hat{s}^i \cdot \hat{t}). \tag{2.25}$$

It then follows from (2.23) that

$$E_t^i + \frac{Z_0}{\eta_o}(\hat{n} \cdot \hat{s}^i)E_t^i - \frac{Z_0}{\eta_o}E_n^i(\bar{t} \cdot \hat{s}^i) = -E_t^r + \frac{Z_0}{\eta_o}(\hat{n} \cdot \bar{s}^i)E_t^r + \frac{Z_0}{\eta_o}(\hat{s}^i \cdot \bar{t})E_n^r. \tag{2.26}$$

In addition, Equation (2.26) can be further simplified if a ray-fixed coordinate system, as shown in Figure 2.6, is used. As shown in Figure 2.6, $\hat{e}_\perp$ is the unit vector perpendicular to the plane of incidence and $\hat{e}^i_{||}$, $\hat{e}^r_{||}$ are the unit vectors parallel to the plane of the incidence and reflection, respectively. After a few manipulations, the relationships between the unit vectors defined in the two previous coordinate systems are

$$\hat{e}_\perp = \hat{b},$$
$$\hat{e}^i_{||} = \hat{t}(\hat{n} \cdot \hat{s}^i) - \hat{n}(\hat{t} \cdot \hat{s}^i),$$
and
$$\hat{e}^r_{||} = -\hat{t}(\hat{n} \cdot \hat{s}^i) - \hat{n}(\hat{t} \cdot \hat{s}^i). \tag{2.27}$$

The normal component (i.e., the component in the $\hat{e}_\perp$ direction) for the reflection coefficient is obtained from (2.24) since the binormal unit vector $\hat{b}$ is in the same

direction as $\hat{e}_{\perp}$. The reflection coefficient for the field components in the parallel $\hat{e}^i_{||}$ and $\hat{e}^r_{||}$ directions (see Figure 2.6) can be obtained by first writing the electric fields as

$$E^{i,r}_{||} = \pm E^{i,r}_t(\hat{n} \cdot \hat{s}^i) - E^{i,r}_n(\hat{t} \cdot \hat{s}^i), \tag{2.28}$$

where the plus sign is for incident electric field at Q_R and the negative sign is for reflected one. Employing Equation (2.26) with (2.27) and (2.28), the reflection coefficient for the parallel field components is

$$E^r_{||}(Q_R) = E^i_{||}(Q_R) \left[\frac{-\frac{Z_0}{\eta_o} + \cos(\theta^i)}{\frac{Z_0}{\eta_o} + \cos(\theta^i)} \right]. \tag{2.29}$$

Thus, by choosing the reflection point Q_R as the phase-reference point, the electric field reflected by the surface S is

$$\bar{E}^r(Q_R) = \bar{\bar{R}} \cdot \bar{E}^i(Q_R) \tag{2.30}$$

where $E^i(Q_R)$ is the electric field incident at Q_R, and $\bar{\bar{R}}$ is the dyadic reflection coefficient in the following matrix notation

$$\bar{\bar{R}} = \begin{bmatrix} R_{||,||} & 0 \\ 0 & R_{\perp,\perp} \end{bmatrix}, \tag{2.31}$$

where

$$R_{||,||} = \left[\frac{-\frac{Z_0}{\eta_o} + \cos(\theta^i)}{\frac{Z_0}{\eta_o} + \cos(\theta^i)} \right],$$

and

$$R_{\perp,\perp} = \left[\frac{-\frac{\eta_o}{Z_0} + \cos(\theta^i)}{\frac{\eta_o}{Z_0} + \cos(\theta^i)} \right]. \tag{2.32}$$

Therefore, the reflected field at Q_R can be easily obtained from Equation (2.30) if a ray-fixed coordinate system is used.

This reflection solution can then be implemented in the NEWAIR Code to calculate reflected-field patterns for an aircraft model. A cross-sectional geometry of an aircraft fuselage with two wings whose surfaces are being modeled by impedance boundary conditions is depicted in Figure 2.7 and used to analyze the reflected-field computations in the code. A coordinate-system transformation on the 2×2 dyadic

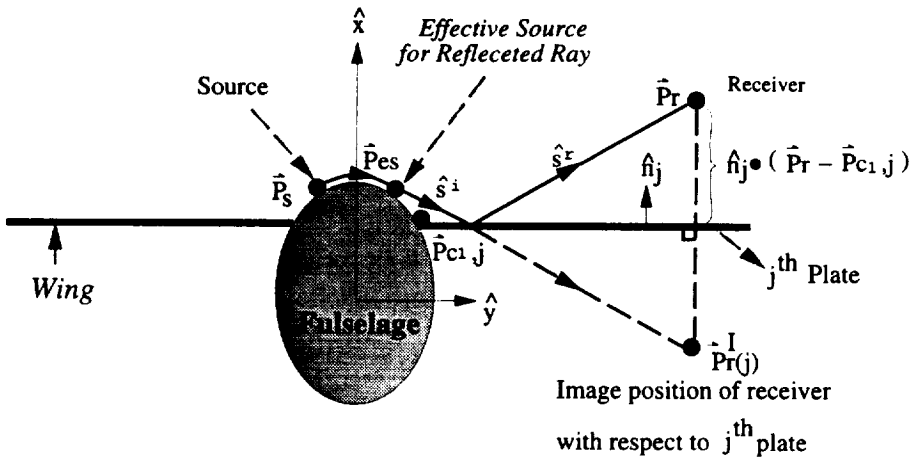

Figure 2.7: Geometry used to determine single-reflected field from an impedance plate.

reflection coefficient in (2.31) is needed since the aircraft code converts every field component to the x, y, and z coordinates in order to add all individual field components easily. The following will briefly describe the reflected-field computations and the modifications of the reflection coefficient in the NEWAIR3 Code.

Before the single-reflected field is computed, the computer code will test blockages of ray paths from a source to the reflection point, and from this point to the receiver. If the rays are not interrupted by any obstacle, then the electric field with only one single reflection point on the surface of a specific plate will be computed by applying image theory.

Consider the cross-sectional geometry of an aircraft fuselage with two wings attached on each side as shown in Figure 2.7. The receiver's image position with respect to the j^{th} plate is given by

$$\bar{P}_r^I(j) = \bar{P}_r - 2\hat{n}_j \cdot (\bar{P}_r - \bar{P}_{c1,j}), \tag{2.33}$$

where the subscript r denotes the reflected field, the superscript I indicates the image position, and the argument j represents the j^{th} plate. The NEWAIR3 Code first calculates the source fields (E_x^s, E_y^s, E_z^s) at the image position $\bar{P}_r^I(j)$. The next step in the computations is to check whether the ray path, from the effective source ($\bar{P}_{es}$) to the image position ($\bar{P}_r^I(j)$), intersects the j^{th} plate. If the given j^{th} plate does not interrupt the ray path, then there is no reflection from this plate to the specific

receiver position. On the other hand, if the ray does intersect the j^{th} plate, then the reflected field (E_x^r, E_y^r, E_z^r) at the receiver location is computed as

$$\begin{bmatrix} E_x^r(\bar{P}_r) \\ E_y^r(\bar{P}_r) \\ E_z^r(\bar{P}_r) \end{bmatrix} = [T] \begin{bmatrix} E_x^s(\bar{P}_r^I(j)) \\ E_y^s(\bar{P}_r^I(j)) \\ E_y^s(\bar{P}_r^I(j)) \end{bmatrix}, \tag{2.34}$$

where the 3×3 transformation $[T]$ matrix has x, y, and z components as follows

$$[T] = \begin{bmatrix} T_{xx} & T_{xy} & T_{xz} \\ T_{yx} & T_{yy} & T_{yz} \\ T_{zx} & T_{zy} & T_{zz} \end{bmatrix}. \tag{2.35}$$

$[T]$ represents the reflected-field polarization transformation matrix and it has to be modified such that it satisfies the impedance boundary conditions (2.21) on the specific j^{th} plate. This $[T]$ matrix is determined by transforming the $E_{||}^r(Q_R)$ and $E_{\perp}^r(Q_R)$ into $E_x^r(Q_R)$, $E_y^r(Q_R)$, and $E_z^r(Q_R)$ field components (i.e., using dot products between the unit vectors $\hat{e}_{||}$, $\hat{e}_{\perp}$ with $\hat{x}$, $\hat{y}$, and $\hat{z}$), namely,

$$[T] = \begin{bmatrix} (\hat{e}_{||}^r \cdot \hat{x}) & (\hat{e}_{\perp} \cdot \hat{x}) \\ (\hat{e}_{||}^r \cdot \hat{y}) & (\hat{e}_{\perp} \cdot \hat{y}) \\ (\hat{e}_{||}^r \cdot \hat{z}) & (\hat{e}_{\perp} \cdot \hat{z}) \end{bmatrix} \cdot \bar{\bar{R}} \cdot \begin{bmatrix} (\hat{e}_{||}^i \cdot \hat{x}) & (\hat{e}_{||} \cdot \hat{y}) & (\hat{e}_{||}^i \cdot \hat{z}) \\ (\hat{e}_{\perp}^i \cdot \hat{x}) & (\hat{e}_{\perp}^i \cdot \hat{y}) & (\hat{e}_{\perp}^i \cdot \hat{z}) \end{bmatrix}, \tag{2.36}$$

where $\bar{\bar{R}}$ is obtained from (2.31). Each element in the $[T]$ matrix can be written in the following form:

$$T_{mn} = R_{||,||}(\hat{e}_{||}^r \cdot \hat{m})(\hat{e}_{||}^i \cdot \hat{n}) + R_{\perp,\perp}(\hat{e}_{\perp} \cdot \hat{m})(\hat{e}_{\perp} \cdot \hat{n}), \tag{2.37}$$

where $\hat{m}$ and $\hat{n}$ denote $\hat{x}$, $\hat{y}$, or $\hat{z}$ unit vectors. Then, the total single-reflected fields $\bar{E}_{total}^r$ of an aircraft model for a given receiver position is the superposition of the single-reflected field from each individual plate, which is obtained from (2.34) and (2.36). The GO field is obtained by adding the total reflected field $\bar{E}_{total}^r$ with the total source field $\bar{E}_{total}^s$ discussed in the previous section. This then completes the GO field solution for the modified aircraft code. If high-order multiple reflected fields are necessary, they can also be added as discussed below.

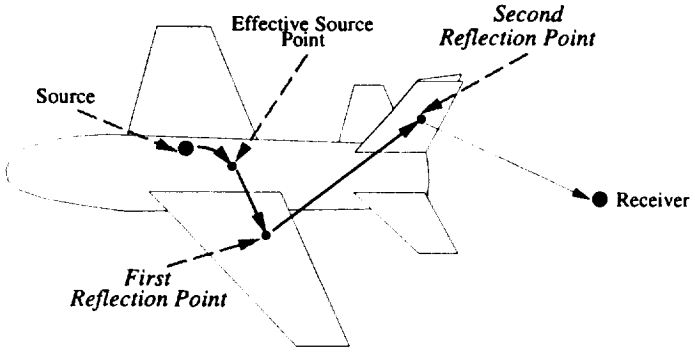

Figure 2.8: Aircraft geometry of an aircraft model for double-reflected field.

2.3 Double-Reflected Field from Flat Coated Surfaces

The procedure for acquiring the single-reflected field (described in the previous section) can be applied here iteratively to obtain the double-reflected field $\bar{E}^{rr}$. Hence, the solution for the double-reflected field can be found by (i) determining the single-reflected field from the first given plate, and (ii) computing the field reflected by the second plate, in which the incident field for the second plate is the reflected field calculated from step (i). This solution can also be implemented in the NEWAIR3 Code to simulate the electric-field patterns for an aircraft model as shown Figure 2.8.

As an illustration, consider a source which is mounted on a perfectly-conducting convex surface with one impedance plate attached to it as depicted in Figure 2.9. The incident rays are first reflected off from the i^{th} plate, and then reflected from the j^{th} plate to the receiver location. The image of the receiver location with respect to the j^{th} plate and i^{th} plate are given, respectively, as follows:

$$\bar{P}_r^I(j) = \bar{P}_r - 2\hat{n}_j \cdot (\bar{P}_r - \bar{P}_{c1,j}),$$

and

$$\bar{P}_r^I(i) = \bar{P}_r^I(j) - 2\hat{n}_i \cdot (\bar{P}_r^I(j) - \bar{P}_{c1,i}). \tag{2.38}$$

The double-reflected field is then calculated by computing the source field $\bar{E}^s$ at the image position $\bar{P}_r^I(i)$ if the double-ly reflected ray is not interrupted by any other

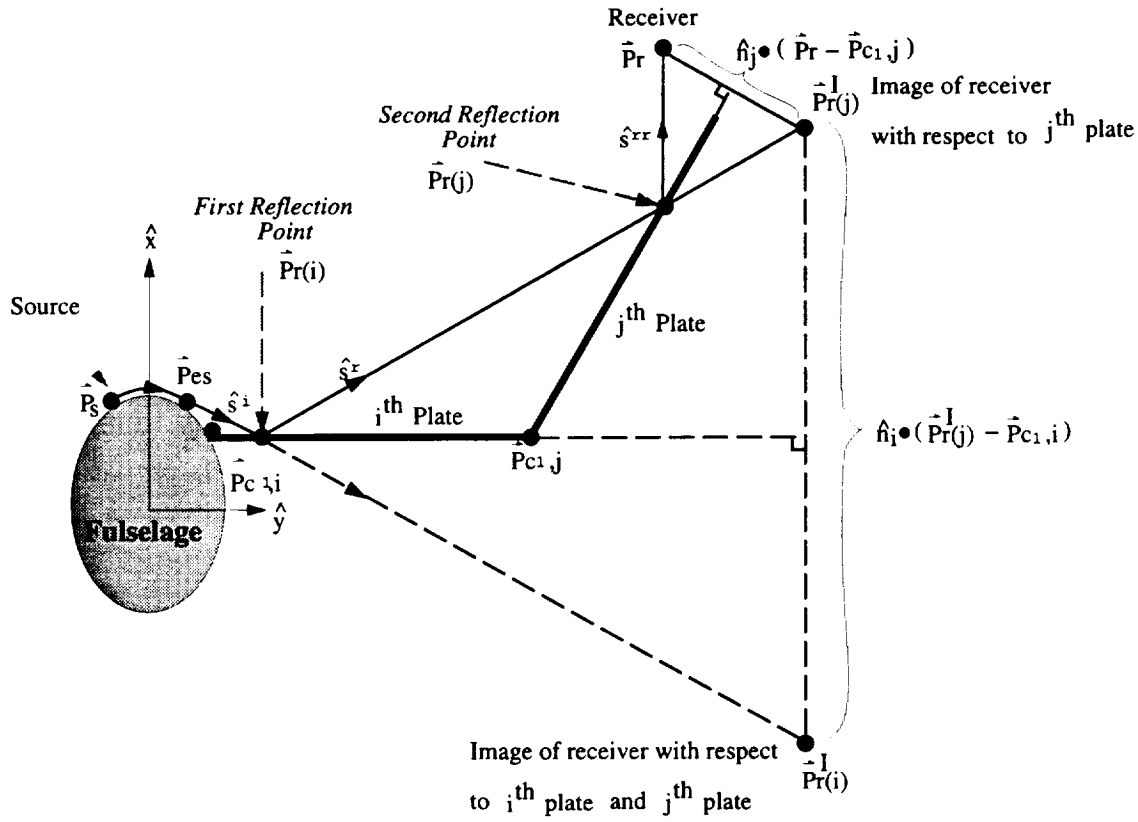

Figure 2.9: Aircraft geometry used to determine double-reflected fields from impedance plates.

structure. Therefore, the double-reflected field $\bar{E}^{rr}$ is computed as

$$\bar{E}^{rr}(\bar{P}_r) = [T]_j [T]_i \left[\bar{E}^s(\bar{P}_r^I(i))\right], \tag{2.39}$$

where $[T]$ matrix is the modified transformation matrix and is defined in equation (2.37). Both $[T]_i$ and $[T]_j$ satisfy the boundary condition (2.21) on the i^{th} and j^{th} plates, respectively. The total electric field reflected twice from the flat plates of the aircraft model is then computed as the sum of each double-reflected field.

Next, due to the fact that the GO fields have discontinuities at the incident and reflection shadow boundaries and are zero in the shadow regions, edge diffracted fields are necessary in order to obtain a more accurate total radiated field. The following chapter will summarize and present the plane-wave edge-diffraction solution for impedance wedges for four specific wedge angles. Modifications of these diffraction solutions for spherical-wave illuminations, which are necessary in the NEWAIR3 Code, will also be discussed at the end of Chapter 3.

Chapter 3

Electromagnetic Diffraction by a Wedge with Impedance Faces for Four Special Cases

It is necessary to include the edge diffracted field to complete the expression for the total electric field in terms of first order terms. This total field is continuous across the shadow boundaries of the GO field, described in Chapter 2; however, it is discontinuous across shadow boundaries of the edge diffracted field because the corner diffracted field is not included. In this chapter, the uniform asymptotic solution for the edge diffracted field due to an impedance wedge, which has been discussed in Rojas [10], is summarized. The incident field in [10] is assumed to be a plane wave with an arbitrary polarization, and obliquely incident to the axis of the wedge. It is noted that for oblique incidence, rigorous solutions have been obtained for only four wedge angles. The primary goal of this chapter is to modify the edge-diffraction solution for plane-wave incidence, so it is also applicable for spherical-wave illumination. This modification is accurate as long as surface waves are neglected.

The method of steepest descents is applied to obtain the uniform solution, and the asymptotic evaluation of the integral representation of the diffracted field is carried out by taking into account of the presence of real geometrical-optics poles. By assuming sources and field locations are far away from the surfaces and edges of impedance wedges which are coated with the lossy impedance material on their surfaces, surface-wave fields can then be neglected here.

Note that $e^{-j\omega t}$ time dependence, which is opposite to $e^{j\omega t}$ used in the GO-field solution discussed in the previous chapter, is assumed and suppressed for all the field expressions described in this chapter. To add this edge diffracted field to the GO field developed in the previous chapter, it is necessary to first take its complex conjugate. In addition, a bar and a double bar on top of a function denote a two-element column vector and a two-by-two matrix, respectively.

3.1 Formulation

The problem considered here is the electromagnetic diffractions by an impedance wedge with a plane-wave incidence (see Figure 3.1). The wedge has an impedance value Z_0 on its 0 face and Z_n on its n face [1]. The external wedge angle is then equal to $n\pi$. Fields on both impedance faces must satisfy the Leontovich or impedance boundary condition

$$\begin{aligned} \vec{E} - \hat{\phi}(\hat{\phi} \cdot \vec{E}) &= \pm\hat{\phi} \times \vec{H} Z_{0,n}, \\ \vec{H} - \hat{\phi}(\hat{\phi} \cdot \vec{E}) &= \mp\hat{\phi} \times \vec{H} Y_{0,n}, \end{aligned} \tag{3.1}$$

$$\phi = \begin{cases} 0 \\ n\pi, \end{cases} \tag{3.2}$$

where $\hat{\phi}$ is the unit vector normal to the plane ϕ, the admittance $Y_{0,n} = 1/Z_{0,n}$, and $\vec{E}$, $\vec{H}$ are electric and magnetic vector fields. As shown in Figure 3.1, a cylindrical coordinate system (ρ, ϕ, z) is used, in which the z axis coincides with the wedge axis. The angles ϕ and ϕ' are both measured from the 0 face of the wedge. The diffraction point Q_E is found by following Keller's law of edge diffraction (i.e., the angle of diffraction β_d is equal to the angle of incident β_0). This can also be represented by

$$\hat{e} \cdot \hat{s}^i = \hat{e} \cdot \hat{s}^d, \tag{3.3}$$

in which $\hat{e}$ is the unit edge vector and $\hat{s}^i$, $\hat{s}^d$ are the incident and diffracted field-propagation directions, respectively.

[1] A wedge is formed by two flat surfaces. The 0 face is considered to be the face where the angles ϕ and ϕ' is measured from. The other face is then called n face.

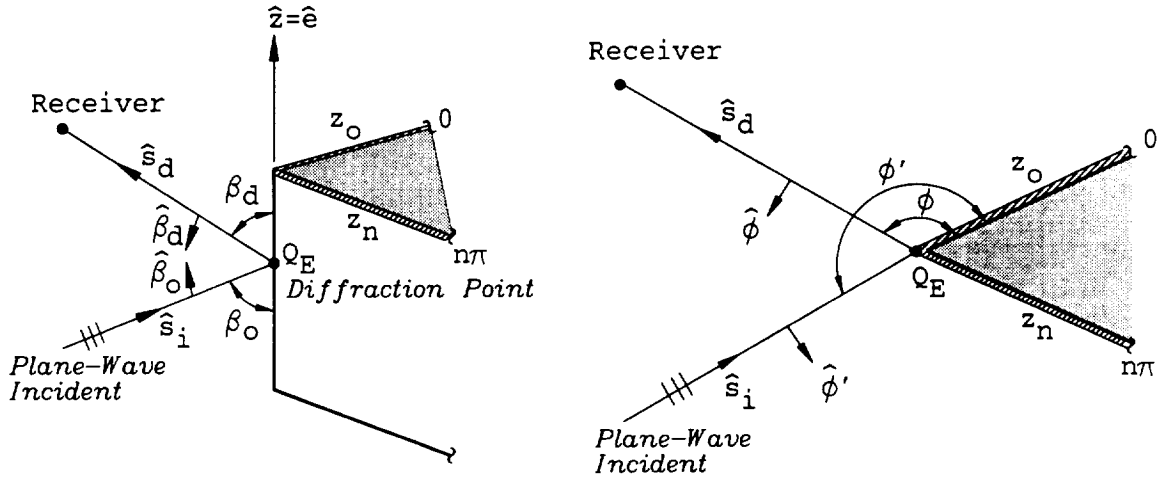

Figure 3.1: Impedance wedge with plane wave obliquely incident on it.

As described in [10], the diffraction solution is based on the generalized reflection method (GRM), which is a generalization of the Maliuzhinets method [9], developed by Vaccaro [14, 15] to investigate fields scattered from an impedance wedge with an obliquely plane wave incident on it. This scattering problem is much more difficult to solve than the normal-incident case, which was considered by Maliuzhinets, since the GRM forms a second-order difference equation, called the Generalized Reflection Equation (GRE), instead of a first-order one. Fortunately, the GRE can be solved in terms of the Maliuzhinets functions for four specific wedge angles. These four special cases are depicted in Figure 3.2(a) to (d) and are listed below [10]:

(i) the half plane ($n = 2$) with an arbitrary impedance value on each face,

(ii) the two-part impedance plane ($n = 1$) with an arbitrary impedance value on each face,

(iii) the right-angled wedge ($n = 3/2$) with a perfect electric conductor (PEC) or a perfect magnetic conductor (PMC) on one face, and

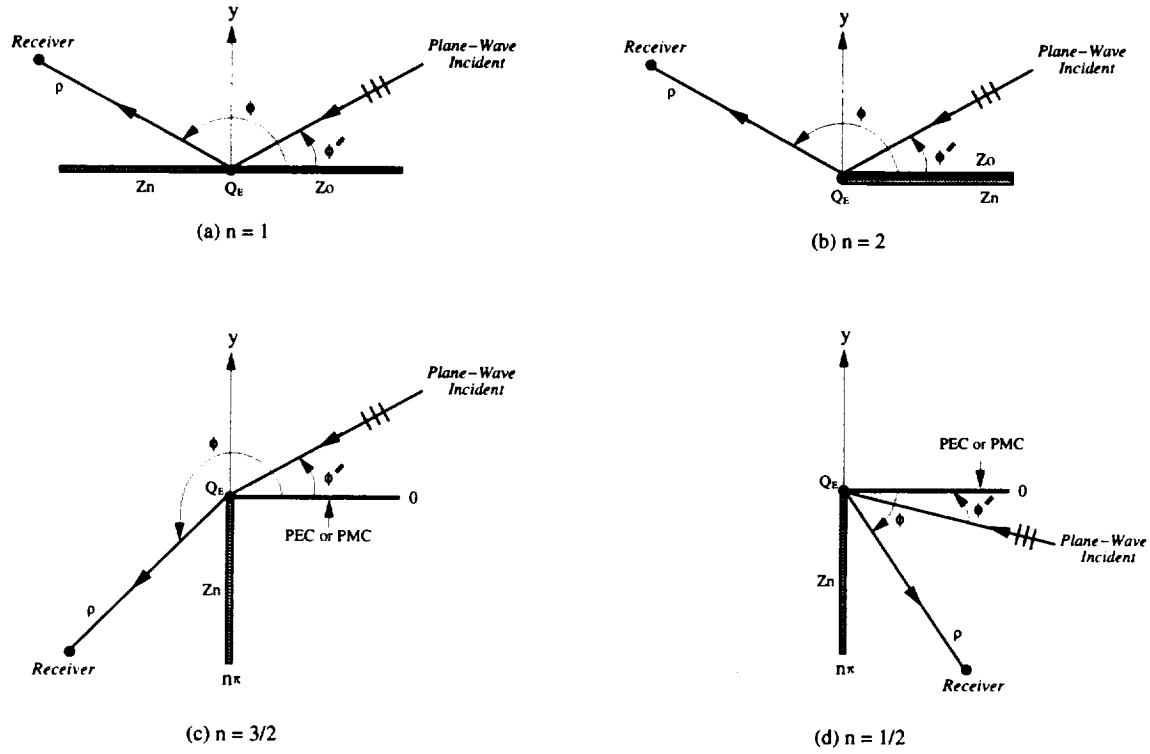

Figure 3.2: Geometries for which the generalized reflection equation has been solved (a) $n = 1$, (b) $n = 2$, (c) $n = 3/2$, and (d) $n = 1/2$.

(iv) the right-angled wedge ($n = 1/2$) with PEC or PMC on one face,

where n is the wedge number and $n\pi$ is the external wedge angle.

Following the Maliuzhinets approach, the total field $\bar{E}_z$ is expressed in terms of a spectrum of plane waves, namely

$$\bar{E}_z(\rho, \phi, z) = \frac{e^{jkz\cos\beta}}{2\pi j} \int_\gamma \bar{F}_z(\alpha + \frac{n\pi}{2} - \phi) e^{-jk\rho\cos\alpha} d\alpha, \tag{3.4}$$

in which $\bar{F}_z$ is the spectral function and γ is the twofold Sommerfeld contour depicted in Figure 3.3. The integral (3.4) can be evaluated in a closed form when $n = 1/2$ as described in [10]. Thus, the following discussion will only concentrate on the solutions for cases of $n = 1, \frac{3}{2}$, and 2 first. The $n = \frac{1}{2}$ case will be discussed at the end of this section.

The spectral function $\bar{F}_z(\alpha)$ can be written as follows

$$\bar{F}_z(\alpha) = \bar{\bar{A}}_z(\alpha) \bar{F}_{oz} \tag{3.5}$$

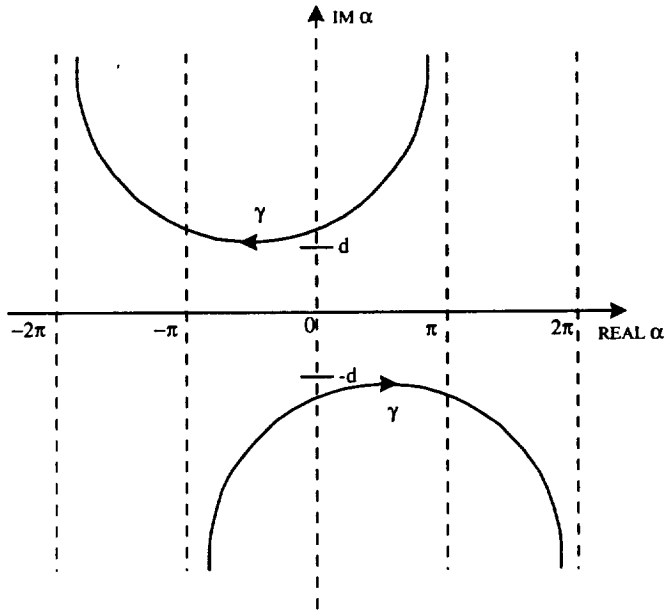

Figure 3.3: Twofold Sommerfeld contour.

where ($\beta \neq 0$) the function $\bar{\bar{A}}_z\,(\alpha)$ is given by

$$\begin{aligned}\bar{\bar{A}}_z\,(\alpha + n\pi/2 - \phi) \;=\; & \bar{\bar{S}}^{-1}\,(\alpha + n\pi/2 - \phi)\cdot \bar{\bar{\Psi}}\,(\alpha + n\pi/2 - \phi)\frac{\sin(\frac{\phi'}{n})}{n} \\ & \left\{ \frac{\bar{\bar{I}}}{\cos(\frac{\alpha-\phi}{n}) - \cos(\frac{\phi'}{n})} + \bar{\bar{B}}_n + \bar{\bar{D}}_n \cos(\frac{\alpha-\phi}{n}) \right\}\cdot \\ & \bar{\bar{\Psi}}^{-1}\,(n\pi/2 - \phi')\,\bar{\bar{S}}\,(n\pi/2 - \phi'), \end{aligned} \tag{3.6}$$

where the 2×2 matrices $\bar{\bar{B}}_n$ and $\bar{\bar{D}}_n$ are given and discussed in Appendix B. When $\beta = \frac{\pi}{2}$ (i.e., the plane wave normally incident upon the impedance wedge), the above function $\bar{\bar{A}}_z$ (3.6) can be simplified as follows

$$\begin{aligned}&\bar{\bar{A}}_z\,(\alpha + n\pi/2 - \phi) = \\ &\quad \bar{\bar{\Psi}}\,(\alpha + n\pi/2 - \phi)\,\bar{\bar{\Psi}}^{-1}\,(n\pi/2 - \phi')\cdot \frac{\frac{\sin(\frac{\phi'}{n})}{n}}{\cos(\frac{\alpha-\phi}{n}) - \cos(\frac{\phi'}{n})}. \end{aligned} \tag{3.7}$$

Unlike the equation (3.6), (3.7) is valid for any wedge angles. This asymptotic evaluation on the diffracted field is based on the work of Gennarelli and Palumbo in [16], and Rojas in [17].

The integral in (3.4) is evaluated asymptotically by applying the method of steepest descents [4] to obtain the leading term of $\bar{E}_z$ for large $k\rho$. By taking into account

of the presence of all poles of $\bar{F}_z$ (3.5) near the saddle points where $\alpha = \pm\pi$, and keeping the leading terms of order $(k\rho)^{-\frac{1}{2}}$, the diffracted field is expressed in terms of the dyadic diffraction coefficient as

$$\bar{E}_z^d(\rho,\phi,z) \sim \bar{\bar{D}}_z\,(\phi,\phi',L,\nu_0,\nu_n)\cdot\bar{E}_z^i(x=0,y=0,z)\frac{e^{jk\rho}}{\sqrt{\rho\sin\beta}}\sin\beta, \tag{3.8}$$

in which the diffraction coefficient $\bar{\bar{D}}_z\ (\rho,\rho',L,\nu_0,\nu_n)$ is (neglecting surface wave poles)

$$\begin{aligned}\bar{\bar{D}}_z\,(\phi,\phi',L,\nu_0,\nu_n) = {} & \frac{e^{j\pi/4}\sin(\frac{\phi'}{n})}{n\sqrt{2\pi k}\sin\beta}\cdot\bar{\bar{S}}^{-1}\,(n\pi/2-\phi)\,\bar{\bar{\Psi}}\,(\pi+n\pi/2-\phi)\\ &\cdot\left\{\begin{array}{l}\dfrac{\bar{\bar{I}}}{\cos(\frac{\pi-\phi}{n})-\cos(\frac{\phi'}{n})}+\bar{\bar{B}}_n+\bar{\bar{D}}_n\cos(\frac{\pi-\phi}{n})\\[2ex] -\bar{\bar{M}}\,(\frac{n\pi}{2}-\phi)\left\{\dfrac{\bar{\bar{I}}}{\cos(\frac{\pi+\phi}{n})-\cos(\frac{\phi'}{n})}+\bar{\bar{B}}_n+\bar{\bar{D}}_n\cos(\frac{\pi+\phi}{n})\right\}\end{array}\right\}\\ &\cdot\bar{\bar{\Psi}}^{-1}\,(n\pi/2-\phi')\,\bar{\bar{S}}\,(n\pi/2-\phi')-\frac{j}{\sqrt{4\pi k}\sin\beta}\cdot\sum_{l=1}^{3}\frac{\bar{\bar{r}}_l\,(1-\mathcal{F}(jkLs_l^2))}{s_l},\end{aligned} \tag{3.9}$$

where $L = \rho\sin\beta$ is the distance parameter. The angles ϕ, ϕ', and β are defined in Figure 3.1. The complex parameters ν_0 and ν_n are related to the surface impedance Z_0 and Z_n, and they are represented as a diagonal matrix (referred as the modified Brewster matrix)

$$\begin{aligned}\sin\bar{\bar{\nu}}_{0,n} &= \begin{bmatrix}\sin\nu_{0,n}^e & 0\\ 0 & \sin\nu_{0,n}^h\end{bmatrix}\\ &= \begin{bmatrix}\frac{\eta_0 Y_{0,n}}{\sin\beta} & 0\\ 0 & \frac{Z_{0,n}}{\eta_0\sin\beta}\end{bmatrix}\end{aligned} \tag{3.10}$$

Due to the fact that $Re(Z_{0,n}) \geq 0$ for passive surfaces, the real part of ν is restricted to an interval between 0 and $\frac{\pi}{2}$.

The function s_l is given by

$$s_l = -e^{\frac{j\pi}{4}}\sqrt{2}\cos\frac{\tilde{\alpha}_l}{2}, \qquad l = 1,\,2,\,3. \tag{3.11}$$

where

$$\tilde{\alpha}_l = \begin{cases}\alpha_l, & \text{if } |Re(\alpha_l)| \leq 2\pi\\ 2\pi + jIm(\alpha_l), & \text{if } Re(\alpha_l) > 2\pi\\ -2\pi + j\alpha_l, & \text{if } Re(\alpha_l) < -2\pi\end{cases} \tag{3.12}$$

and the poles α_l for $l = 1, 2, 3$, are defined as

$$\alpha_1 = \phi - \phi',$$
$$\alpha_2 = \phi + \phi',$$
and
$$\alpha_3 = \phi + \phi' - 2n\pi. \tag{3.13}$$

The residues $\bar{\bar{r}}_l$ inside the summation in (3.9) are

$$\bar{\bar{r}}_l = \lim_{\alpha \to \alpha_l} (\alpha - \alpha_l)\, \bar{\bar{A}}_z\, (\alpha + \frac{n\pi}{2} - \phi), \qquad \text{l=1,2,3} \tag{3.14}$$

in which the poles α_l are given in (3.13) and $\bar{\bar{A}}_z\, (\alpha + \frac{n\pi}{2} - \phi)$ is defined in (3.6) for an obliquely-incident field and (3.7) for a normally-incident field.

The function $\mathcal{F}(x)$ introduced in (3.9) is the transition function with a complex argument (according to [18, 4])

$$\mathcal{F}(x) = 2j\sqrt{x}e^{jx} \int_{\sqrt{x}}^{\infty} e^{-jt^2} dt \qquad -\frac{3\pi}{2} < x < \frac{\pi}{2}. \tag{3.15}$$

The argument x is restricted to the interval $-\frac{3\pi}{2} < x < \frac{\pi}{2}$ to assure that $\mathcal{F}(x)$ is a single-valued function, and it converges as $|x| \to \infty$. The matrix $\bar{\bar{I}}$ in (3.9) is a 2×2 identity matrix. The matrix $\bar{\bar{\Psi}}$ can be expressed as a 2x2 diagonal matrix

$$\bar{\bar{\Psi}}\, (\alpha) = \begin{bmatrix} \Psi_e(\alpha) & 0 \\ 0 & \Psi_h(\alpha) \end{bmatrix}, \tag{3.16}$$

in which $\Psi_{e,h}(\alpha)$ is written as a product of four Maliuzhinets functions,

$$\begin{aligned} \Psi_{e,h}(\alpha) \;=\; & \psi_n(\alpha + \frac{n\pi}{2} + \nu_0^{e,h} - \frac{\pi}{2})\psi_n(\alpha + \frac{n\pi}{2} - \nu_0^{e,h} + \frac{\pi}{2}) \\ & \cdot\psi_n(\alpha - \frac{n\pi}{2} + \nu_n^{e,h} - \frac{\pi}{2})\psi_n(\alpha - \frac{n\pi}{2} - \nu_n^{e,h} + \frac{\pi}{2}). \end{aligned} \tag{3.17}$$

The Maliuzhinets function $\psi(\alpha)$ and its properties are discussed in Maliuzhinets [9]. Note that one of the important identities given in [9], which was used to develop the diffracted field is

$$\bar{\bar{\Psi}}\, (\alpha - \pi) = \bar{\bar{\Psi}}\, (\alpha + \pi)\, \bar{\bar{M}}\, (\alpha), \tag{3.18}$$

in which the diagonal matrix $\bar{\bar{M}}\, (\alpha)$ is given by

$$\bar{\bar{M}}\, (\alpha) \;=\; \begin{bmatrix} M_e(\alpha) & 0 \\ 0 & M_h(\alpha) \end{bmatrix}$$

$$M_{e,h}(\alpha) = \frac{m(\alpha, \nu_0^{e,h})}{m(-\alpha, \nu_n^{e,h})}, \tag{3.19}$$

where

$$m(\alpha, \nu) = \frac{\cos(\frac{\alpha+n\pi/2-\nu}{2n})\cos(\frac{\alpha-\pi+n\pi/2+\nu}{2n})}{\cos(\frac{\alpha+n\pi/2+\nu}{2n})\cos(\frac{\alpha+\pi+n\pi/2-\nu}{2n})}. \tag{3.20}$$

The matrix $\bar{\bar{S}}$ is the transformation matrix which converts the fields that are tangent to the wedge walls (i.e., $\hat{z}$ direction) to the normal component of the fields. The matrices $\bar{\bar{B}}_n$ and $\bar{\bar{D}}_n$ are included in order to remove the singularities caused by the inverse of $\bar{\bar{S}}$ (see (3.9)) and to satisfy the edge condition. The expressions for $\bar{\bar{S}}(\alpha)$, $\bar{\bar{\Psi}}(\alpha)$, $\bar{\bar{M}}(\alpha)$, and $\bar{\bar{r}}_l$ will be discussed and defined for each of the special cases in the following sections. The computation of the matrices $\bar{\bar{B}}_n$ and $\bar{\bar{B}}_n$ is discussed in Appendix B.

The ray-fixed coordinate system (as shown in Figure 3.1) is used to express the diffracted field [4]. Thus, the diffracted field $\bar{E}^d$ in the vector form with $\hat{\beta}$ and $\hat{\phi}$ components is

$$\bar{E}^d = \begin{bmatrix} \bar{E}_\beta^d \\ \bar{E}_\phi^d, \end{bmatrix} \tag{3.21}$$

in which the unit vectors $\hat{e}$, $\hat{\beta}$, $\hat{\phi}$, $\hat{\beta}'$, and $\hat{\phi}'$ are depicted in Figure 3.1 and are defined as follows [10]:

$$\begin{aligned} &\hat{e} = \hat{z}, \\ &\hat{\beta} = \hat{\phi} \times \hat{s}, \\ &\hat{\beta}' = \hat{\phi}' \times \hat{s}', \\ &\hat{\phi} = -\frac{\hat{s} \times \hat{e}}{|\hat{s} \times \hat{e}|}, \\ &\text{and} \\ &\hat{\phi}' = \frac{\hat{s}' \times \hat{e}}{|\hat{s}' \times \hat{e}|}. \end{aligned} \tag{3.22}$$

The expression for the diffracted field $\bar{E}^d$ can then be obtained from (3.8) and (3.9), namely,

$$\bar{E}^d(s, \phi, \beta) \sim \bar{\bar{D}}_e(\phi, \phi', \beta, L, \nu_0, \nu_n)\bar{E}^i(Q_E)\frac{e^{jks}}{\sqrt{s}}, \tag{3.23}$$

where $\bar{E}^i(Q_E)$ is the incident field at the diffraction point Q_E, s is the distance from Q_E to the observation point, and the distance parameter $L = s\sqrt{\sin\beta}$. The diffraction

coefficient $\bar{\bar{D}}_e$ is given by

$$\bar{\bar{D}}_e(\phi,\phi',\beta,L,\nu_0,\nu_n) = -\bar{\bar{L}}\bar{\bar{D}}_z(\phi,\phi',\beta,L,\nu_0,\nu_n)\bar{\bar{L}}, \tag{3.24}$$

where

$$\bar{\bar{L}} = \begin{bmatrix} 1 & 0 \\ 0 & -1 \end{bmatrix}. \tag{3.25}$$

Unlike the cases discussed above for $n = 1, \frac{3}{2}$, and 2, the integral in (3.4) can be evaluated in a closed form for $n = 1/2$. As described in [10], the spectral function $\bar{F}_z$ in (3.4) has a period of 2π for $n = 1/2$; hence, the two integrals represented the diffracted field canceled with each other. The result is that the diffracted field for the cases of $n = 1/2$ (i.e., with the external wedge angle of $\pi/2$) is zero.

The diffracted field discussed here has an order $(k\rho)^{\frac{-1}{2}}$ with respect to the incident field. In order to obtain more accurate diffracted fields on the faces of the impedance wedge for finite nonzero values of $Z_{0,n}$, it is necessary to include the next higher order term $(k\rho)^{\frac{-3}{2}}$ as described in Tiberio and Manara [19, 20]. The expressions for the diffracted fields in (3.8) and (3.23) are valid as long as all the poles α_l in (3.13) are simple. In the cases that grazing incident $\phi' = 0, n\pi$, or $\phi = 0, n\pi$, or $Z_{0,n} = 0$ or ∞, there is a possibility of double or higher order poles. In these cases, special manipulations on the integral (3.4) must be carried out as described in [10]. In the following sections, the expressions for $\bar{\bar{S}}(\alpha)$, $\bar{\bar{\Psi}}(\alpha)$, $\bar{\bar{M}}(\alpha)$, and $\bar{\bar{r}}_l$ will be discussed and defined for each special case.

3.1.1 Transformation Matrix $\bar{\bar{S}}(\alpha)$

The diffracted field presented in the last section can be written as

$$\bar{\bar{S}}^{-1}\,[\text{Diffraction Coefficient}]\,\bar{\bar{S}}\,\bar{E}^i_z(Q_E). \tag{3.26}$$

There are three steps in order to obtain Equation (3.26):

(i) multiply $\bar{E}^i_z(Q_E)$ with $\bar{\bar{S}}$ to obtain an intermediate expression, which is proportional to the normal incident-field component which is perpendicular to the wedge wall,

(ii) multiply $\bar{\bar{S}}\ \bar{E}_z^i(Q_E)$ with the diffraction coefficient to obtain the "normal" component of the diffracted field $\bar{E}^d_{normal}$,

(iii) multiply the inverse of $\bar{\bar{S}}$ by $\bar{E}^d_{normal}$ to obtain the diffracted-field component $\bar{E}^d_z$.

The expression for $\bar{\bar{S}}$ is written in terms of the matrix $\bar{\bar{C}}$ as

$$\bar{\bar{S}}= \begin{cases} \bar{\bar{C}}\,(\alpha - \frac{\pi}{2}), & \text{for n=1} \\ \bar{\bar{C}}\,(\alpha), & \text{for n=2} \\ \bar{\bar{C}}\,(\alpha + \frac{n\pi}{2}), & \text{for } n = \frac{3}{2}, \frac{1}{2} \text{ and } Z_0 = 0 \text{ or } Z_0 = \infty \end{cases}, \tag{3.27}$$

where

$$\bar{\bar{C}}\,(\alpha) = \bar{\bar{I}}\cos(\alpha) + \bar{\bar{J}}\cos(\beta),$$

$$\bar{\bar{I}}= \begin{bmatrix} 1 & 0 \\ 0 & 1 \end{bmatrix},$$

and

$$\bar{\bar{J}}= \begin{bmatrix} 0 & -1 \\ 1 & 0 \end{bmatrix}. \tag{3.28}$$

3.1.2 Residues $\bar{\bar{r}}_l$

The $\bar{\bar{r}}_l, l = 1,2,3$ are the residues of $\bar{\bar{A}}_z\ (\alpha + n\pi/2 - \phi)$ given in equation (3.6) and (3.7), and are computed in (3.14). The following summarizes the expressions for the residues:

$$\bar{\bar{r}}_1=\bar{\bar{I}},$$

$$\bar{\bar{r}}_2= \begin{cases} \bar{\bar{C}}^{-1}\,(\pi + \phi')\,\bar{\bar{\Lambda}}\,(\phi', \nu_0)\,\bar{\bar{C}}\,(\pi - \phi'), & \text{n = 1, 2} \\ -\,\bar{\bar{C}}^{-1}\,(\frac{3\pi}{2} + \phi')\,\bar{\bar{\Lambda}}_1\bar{\bar{C}}\,(\frac{3\pi}{2} - \phi'), & \text{n = 3/2} \end{cases}$$

and

$$\bar{\bar{r}}_3= \begin{cases} \bar{\bar{C}}^{-1}\,(\pi + \phi')\,\bar{\bar{\Lambda}}\,(n\pi - \phi', \nu_n)\,\bar{\bar{C}}\,(\pi - \phi'), & \text{n = 1, 2} \\ \bar{\bar{C}}^{-1}\,(\phi' - \frac{3\pi}{2})\,\bar{\bar{\Lambda}}\,(n\pi - \phi', \nu_n)\,\bar{\bar{C}}\,(\frac{3\pi}{2} - \phi'). & \text{n = 3/2} \end{cases} \tag{3.29}$$

The functions $\bar{\bar{\Lambda}}(\alpha,\nu)$ and $\bar{\bar{\Lambda}}_1$ are given as follows:

$$\begin{aligned}\bar{\bar{\Lambda}}(\alpha,\nu) &= \begin{bmatrix} R(\alpha,\nu^e) & 0 \\ 0 & R(\alpha,\nu^h) \end{bmatrix}, \\ \bar{\bar{\Lambda}}_1 &= \begin{cases} -\bar{\bar{L}}, & \text{for } Z_0 = 0 \\ \bar{\bar{L}}, & \text{for } Z_0 = \infty \end{cases}\end{aligned} \tag{3.30}$$

where

$$R(\alpha,\nu) = \frac{\sin(\alpha) - \sin(\nu)}{\sin(\alpha) + \sin(\nu)}, \tag{3.31}$$

and $\bar{\bar{L}}$ is defined in (3.25).

3.1.3 Limits on Matrices $\bar{\bar{\Psi}}(\alpha)$ and $\bar{\bar{M}}(\alpha)$

In this section, the matrices $\bar{\bar{M}}(\alpha)$ and $\bar{\bar{\Psi}}(\alpha)$ are summarized in tables 3.1, 3.2, and 3.3 for the special cases where the impedance value Z_0 or Z_n goes to zero or infinity. For both Z_0 and Z_n are finite, $\bar{\bar{M}}(\alpha)$ and $\bar{\bar{\Psi}}(\alpha)$ are already defined in (3.19) and (3.16). The relationship between the two matrices is given in (3.18).

As the impedance value Z_0 or Z_n approaches zero or infinity, the complex arguments ν^e and ν^h defined in (3.10) become:

$$\begin{aligned}&\lim_{Z_0\to 0} \begin{cases} |\nu_0^e| \to \infty \\ \nu_0^h \to 0 \end{cases}, \\ &\lim_{Z_n\to 0} \begin{cases} |\nu_n^e| \to \infty \\ \nu_n^h \to 0 \end{cases}, \\ &\text{and} \\ &\lim_{Z_0\to \infty} \begin{cases} \nu_0^e \to 0 \\ \left|\nu_0^h\right| \to \infty \end{cases}.\end{aligned} \tag{3.32}$$

The $\Psi_{e,h}(\alpha)$ defined in (3.17) can be simplified by applying one of the Maliuzhinets identities given in [9]

$$\lim_{|Im(\alpha)|\to\infty} \psi_n(\alpha) = 0\left[e^{\frac{|Im(\alpha)|}{4n}}\right]. \tag{3.33}$$

Employing the above limits to the equations (3.16) and (3.19) as the $|Im(\alpha)|$ goes to infinity, the following tables summarize the simplified $\Psi_{e,h}(\alpha)$ and $M_{e,h}(\alpha)$ for the four special cases.

Table 3.1: $n = 1, 2$ for $\Psi_{e,h}(\alpha)$

$Z_0 = 0$,	$\Psi_e(\alpha) = \psi_n(\alpha - \frac{n\pi}{2} + \nu_n^e - \frac{\pi}{2})\psi_n(\alpha - \frac{n\pi}{2} - \nu_n^e + \frac{\pi}{2})$
$Z_n \neq 0$ and finite,	$\Psi_h(\alpha) = \cos(\frac{\alpha}{2n} + \frac{\pi}{4})\psi_n(\alpha - \frac{n\pi}{2} + \nu_n^h - \frac{\pi}{2})\psi_n(\alpha - \frac{n\pi}{2} - \nu_n^h + \frac{\pi}{2})$
$Z_0 \neq 0$ and finite,	$\Psi_e(\alpha) = \psi_n(\alpha + \frac{n\pi}{2} + \nu_0^e - \frac{\pi}{2})\psi_n(\alpha + \frac{n\pi}{2} - \nu_0^e + \frac{\pi}{2})$
$Z_n = 0$,	$\Psi_h(\alpha) = \cos(\frac{\alpha}{2n} - \frac{\pi}{4})\psi_n(\alpha + \frac{n\pi}{2} + \nu_0^h - \frac{\pi}{2})\psi_n(\alpha + \frac{n\pi}{2} - \nu_0^h + \frac{\pi}{2})$
$Z_0 = 0$,	$\Psi_e(\alpha) = 1$
$Z_n = 0$,	$\Psi_h(\alpha) = \cos(\frac{\alpha}{2n} + \frac{\pi}{4})\cos(\frac{\alpha}{2n} - \frac{\pi}{4})$
$Z_0 = \infty$,	$\Psi_e(\alpha) = \cos(\frac{\alpha}{2n} + \frac{\pi}{4})\psi_n(\alpha - \frac{n\pi}{2} + \nu_n^e - \frac{\pi}{2})\psi_n(\alpha - \frac{n\pi}{2} - \nu_n^e + \frac{\pi}{2})$
$Z_n \neq 0$ and finite.	$\Psi_h(\alpha) = \psi_n(\alpha - \frac{n\pi}{2} + \nu_n^h - \frac{\pi}{2})\psi_n(\alpha - \frac{n\pi}{2} - \nu_n^h + \frac{\pi}{2})$

Table 3.2: $n = \frac{1}{2}, \frac{3}{2}$ for $\Psi_{e,h}(\alpha)$

$Z_0 = 0$,	$\Psi_e(\alpha) = \cos(\frac{\alpha}{2n} + \frac{\pi}{4})\psi_n(\alpha - \frac{n\pi}{2} + \nu_n^e - \frac{\pi}{2})\psi_n(\alpha - \frac{n\pi}{2} - \nu_n^e + \frac{\pi}{2})$
$Z_n \neq 0$ and finite,	$\Psi_h(\alpha) = \psi_n(\alpha - \frac{n\pi}{n} + \nu_n^h - \frac{\pi}{2})\psi_n(\alpha - \frac{n\pi}{2} - \nu_n^h + \frac{\pi}{2})$
$Z_0 \neq 0$ and finite,	$\Psi_e(\alpha) = \cos(\frac{\alpha}{2n} - \frac{\pi}{4})\psi_n(\alpha + \frac{n\pi}{2} + \nu_0^e - \frac{\pi}{2})\psi_n(\alpha + \frac{n\pi}{2} - \nu_0^e + \frac{\pi}{2})$
$Z_n = 0$,	$\Psi_h(\alpha) = \psi_n(\alpha + \frac{n\pi}{2} + \nu_0^h - \frac{\pi}{2})\psi_n(\alpha + \frac{n\pi}{2} - \nu_0^h + \frac{\pi}{2})$
$Z_0 = 0$,	$\Psi_e(\alpha) = \cos(\frac{\alpha}{2n} + \frac{\pi}{4})\cos(\frac{\alpha}{2n} - \frac{\pi}{4})$
$Z_n = 0$,	$\Psi_h(\alpha) = 1$
$Z_0 = \infty$,	$\Psi_e(\alpha) = \psi_n(\alpha - \frac{n\pi}{2} + \nu_n^e - \frac{\pi}{2})\psi_n(\alpha - \frac{n\pi}{2} - \nu_n^e + \frac{\pi}{2})$
$Z_n \neq 0$ and finite.	$\Psi_h(\alpha) = \cos(\frac{\alpha}{2n} + \frac{\pi}{4})\psi_n(\alpha - \frac{n\pi}{2} + \nu_n^h - \frac{\pi}{2})\psi_n(\alpha - \frac{n\pi}{2} - \nu_n^h + \frac{\pi}{2})$

3.2 Modification for Spherical-Wave Illumination

Finally, in order to apply the above edge diffraction solution for impedance wedges to the NEWAIR3 Code, modifications on some parameters must be made. Since the incident field was assumed to be a plane wave for the previously described edge diffractions, the solution has to be modified for a point source which is compatible with the aircraft code. The distance parameter L inside the argument of the transition function $\mathcal{F}(x)$ (3.15) has to be replaced by the following expression:

$$L = \frac{s^d(s^i + l)}{s^d + s^i + l}\sin^2(\beta_0), \tag{3.34}$$

Table 3.3: $n = 1, 2, \frac{1}{2}, \frac{3}{2}$ for $M_{e,h}(\alpha)$

$Z_0 = 0,$ $Z_n \neq 0$and finite,	$M_e(\alpha) = \frac{\cos(\frac{\alpha-\pi+n\pi/2}{2n})}{m(-\alpha,\nu_n^e)\cos(\frac{\alpha+\pi+n\pi/2}{2n})}$ $M_h(\alpha) = \frac{1}{m(-\alpha,\nu_n^h)}$
$Z_0 \neq 0$ and finite, $Z_n = 0,$	$M_e(\alpha) = \frac{m(\alpha,\nu_0^e)\cos(\frac{-\alpha+\pi+n\pi/2}{2n})}{\cos(\frac{-\alpha-\pi+n\pi/2}{2n})}$ $M_h(\alpha) = m(\alpha,\nu_0^h)$
$Z_0 = 0,$ $Z_n = 0,$	$M_e(\alpha) = \frac{\cos(\frac{\alpha-\pi+n\pi/2}{2n})\cos(\frac{-\alpha+\pi+n\pi/2}{2n})}{\cos(\frac{\alpha+\pi+n\pi/2}{2n})\cos(\frac{-\alpha-\pi+n\pi/2}{2n})}$ $M_h(\alpha) = 1$
$Z_0 = \infty,$ $Z_n \neq 0$ and finite,	$M_e(\alpha) = \frac{1}{m(-\alpha,\nu_n^e)}$ $M_h(\alpha) = \frac{\cos(\frac{\alpha-\pi+n\pi/2}{2n})}{m(-\alpha,\nu_n^h)\cos(\frac{\alpha+\pi+n\pi/2}{2n})}$

where s^i shown in Figure 3.4 is the distance from the effective source point[2] to the diffraction point, and s^d in Figure 3.4 is the distance from the diffraction point to the receiver location. The angle β is the angle between the incident ray and the edge where the diffractions occur. Another parameter which also depends on the types of the sources is the spatial attenuation factor A. For the plane-wave incident case, A is equal to $1/\sqrt{\rho}$ in (3.23); however, the spatial attenuation factor has the following expression if a point source is considered:

$$A = \sqrt{\frac{s^i}{s^d(s^d + s^i)}}, \tag{3.35}$$

where s^i and s^d have the same definitions as above and are depicted in Figure 3.4.

Following all the modifications for the edge diffraction solution, the implementation of impedance plates in the NEWAIR3 Code can then be completed. The following chapter will present and discuss the computer simulated results for various aircraft models with impedance wings.

[2]If the receiver is determined to be in the lit region, then the effective source point is the same as the actual source point. However, if the field point is in the shadow region, then rays travel an extra distance l from the actual source point to a point where the rays diffract. In addition, this point is then the effective source point.

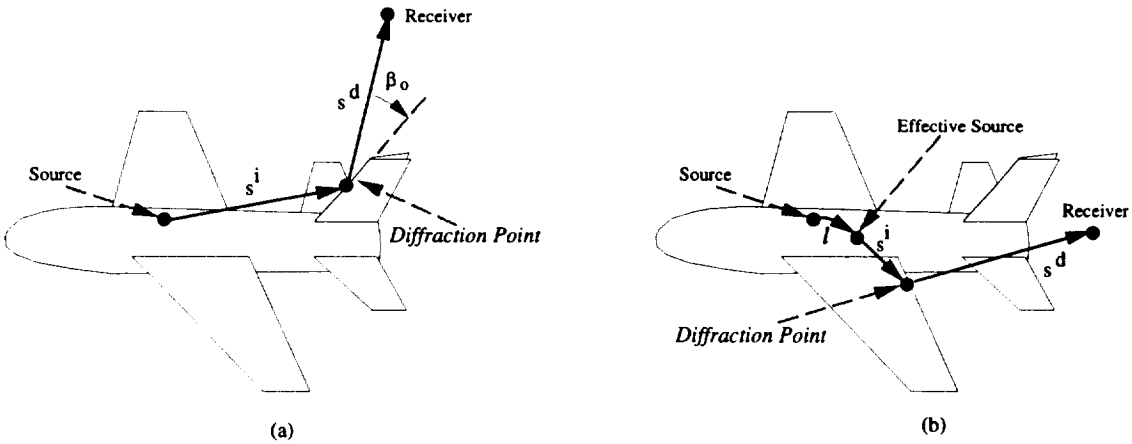

Figure 3.4: Geometry of an aircraft model for edge diffraction with the diffraction point (a) in the lit region, and (b) in the shadow region.

Chapter 4

Computer Simulations and Discussions

The purpose of this chapter is to implement the modified plane-wave solutions, which are discussed in Chapters 2 and 3, to study the effects of the composite plates which are newly introduced to the NEWAIR3 Code. In most applications, the aircraft distorts the desired pattern of the antenna. Thus, the examples here will show that the undesired reflected and diffracted fields can be minimized by choosing the right surface impedance values for the plates. As mentioned before, the composite plates are being modeled by impedance plates. The numerical results will include two main parts : (i) the plane-wave incident cases, and (ii) the NEWAIR3 Code cases. For the plane-wave incident cases, the behavior of both the reflected and diffracted fields as functions of the surface impedances and the observation angles are investigated. On the other hand, seven examples including three ellipsoid-plate geometries are simulated with the modified NEWAIR3 Code. For the purpose of assessing the validity of the diffraction solutions discussed in Chapter 3, the first example will show the individual first-order field component and the approximated first-order total field. Other test examples will mainly emphasize improving the radiation patterns. The simulation results will be discussed and compared to the results from the original NEWAIR3 Code. Note that the lit-side impedance is denoted as Z_0, and Z_n is referred as the shadow-side impedance.

4.1 Plane-Wave Case

This section will discuss and investigate how the surface impedance will affect the reflected and diffracted fields. The source field is assumed to be a plane wave. The surface impedances used for all plots of the plane-wave incident cases are normalized with respect to the free-space intrinsic impedance $\eta_0 \approx 377\ \Omega$, and also the real parts of the impedances are assumed to be positive.

4.1.1 The Reflected Field

Consider a geometry of a parallel-polarized plane wave[1] incident upon the lit side of an impedance ground plane with an incident angle[2] $\theta^i = 60$ degree as depicted in Figure 4.1(a). According to Equation (2.31), the reflected field is decoupled such that it has the same polarization direction as the incident field. The field amplitude of the parallel-polarized reflected field is plotted as a function of the surface impedance as shown in Figure 4.2(a). As both the real and the imaginary parts of the surface impedance varied, the minimum reflected field can be found at $Z_0 \approx 0.5 * \eta_0\ \Omega$. It is noted that the surface impedance corresponding to the smallest field magnitude will be referred as the "optimal" impedance for all numerical examples. Thus, $0.5 * \eta_0\ \Omega$ is the "optimal" impedance for this parallel-reflected field example where $\theta^i = 60°$.

The next case will consider the perpendicular-polarized incident field for the same impedance ground plane, as shown in Figure 4.1(b). The incident angle θ^i is still fixed at 60 degrees. The perpendicular-polarized reflected field as a function of the surface impedance is calculated and obtained in Figure 4.2(b). The "optimal" impedance value for this case is approximately equal to $Z_0 = 2 * \eta_0\ \Omega$. Note that the imaginary part of the "optimal" impedance values is fairly small in both the reflected-field cases.

[1] A parallel plane wave is an electric field which is polarized in the direction parallel to the plane of incidence.

[2] The incident angle θ^i is measured from the normal $\hat{n}$ of the ground plane.

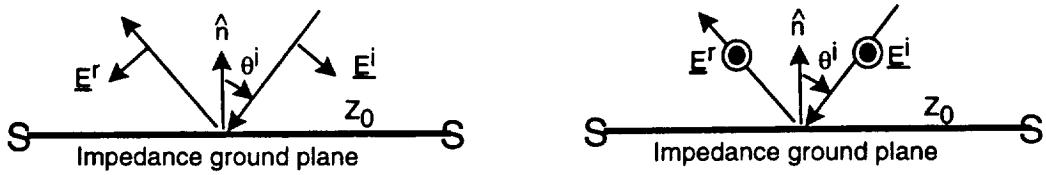

(a) (b)

Figure 4.1: Geometry of a (a) parallel and (b) perpendicular -polarized plane waves incident on an impedance ground plane.

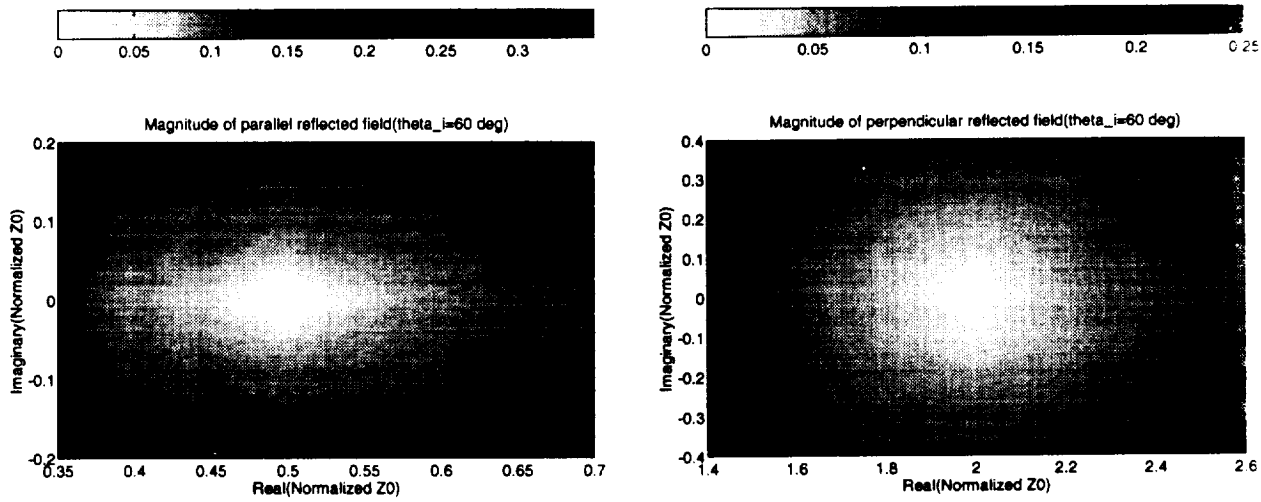

(a) (b)

Figure 4.2: Amplitude distribution of single-reflected field with (a) $E^i_{||}$ and (b) $E^i_{\perp}$ incident upon an impedance ground plane at $\theta^i = 60$ degrees.

4.1.2 The Edge-Diffracted Field

Following the reflected-field cases, this section will investigate the edge-diffracted fields as functions of the surface impedances and the observation angles. The geometry considered here is a half plane with the surface impedance Z_0 on its lit face and $Z_n = (0.1 + j0.5)$ on its opposite face. The axis of the half plane is assumed to coincide with the $\hat{z}$ axis as shown in Figure 3.1. A TM_z or a TE_z plane wave is assumed to be incident upon the impedance half plane and makes a diffraction angle[3] of 135 degrees with respect to the $\hat{z}$ axis. The incident angle ϕ_i measured from lit face of the impedance half plane is assumed to be 45 degrees. The diffracted field is calculated at a distance $k\rho = 10$ where k is the free-space wave number, and ρ is the distance between the diffraction point on the edge and the field location. The following will discuss the TM_z and TE_z cases separately.

(i) TM_z Plane-Wave Incident:

The TM_z case shown in Figure 4.3 is considered first. With the observation angle fixed at 60 degrees, the co-polarized and cross-polarized diffracted fields are calculated and plotted as functions of the surface impedance Z_0 as shown in Figure 4.4(a) and Figure 4.4(b), respectively. The co-polarized diffracted field has a minimum at $Z_0 \approx 0.5 * \eta_0\ \Omega$ according to Figure 4.4(a). On the other hand, Figure 4.4(b) shows the cross-polarized field component has an "optimal" impedance located at $Z_0 \approx (1.3 + j0.1) * \eta_0\ \Omega$. Note that the magnitude of the cross-polarized field is fairly small at $Z_0 = 0$ (i.e., the lit side of the half plane is a PEC).

Next, the diffracted field as a function of observation angles is investigated in this TM_z-incident example. The same geometry as depicted in Figure 4.3 is considered, except the observation angle ϕ is varied from 0 to 360 degrees and also the lit-side impedance Z_0 is assumed to be real and varied from 0 to $1 * \eta_0\ \Omega$. Figure 4.5(a) and Figure 4.5(b) show the co-polarized and cross-polarized diffracted fields as functions of the observation angles. Five curves

[3]Please refer to Figure 3.1 for the definition of the diffraction angle β_d

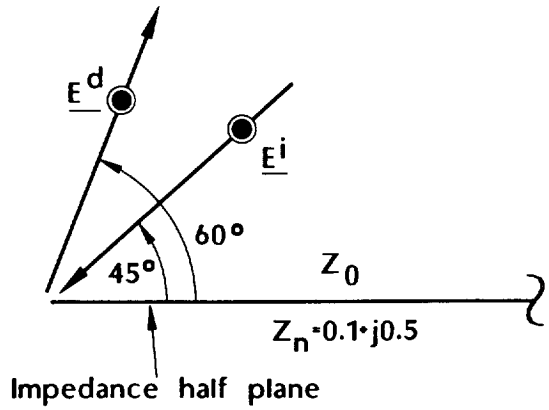

Figure 4.3: Geometry of TM_z plane wave incident upon an impedance half plane with a 135-degree diffraction angle measured from the axis of the half plane.

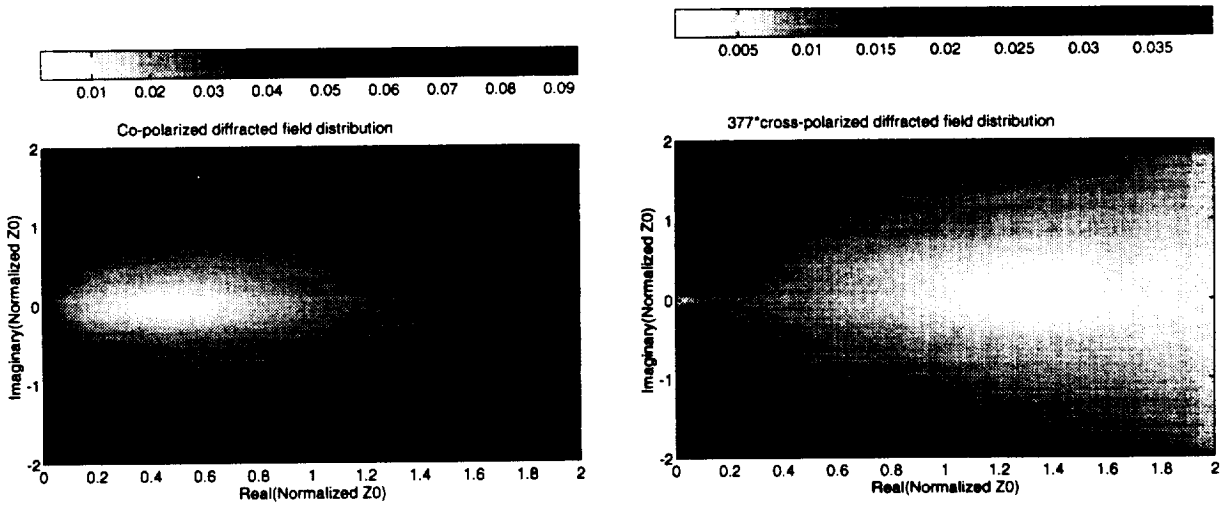

(a) (b)

Figure 4.4: Amplitude distributions of the (a) co-polarized E_z^d and (b) cross-polarized $\eta_0 H_z^d$ edge-diffracted fields with E_z^i incident upon an impedance half plane. .

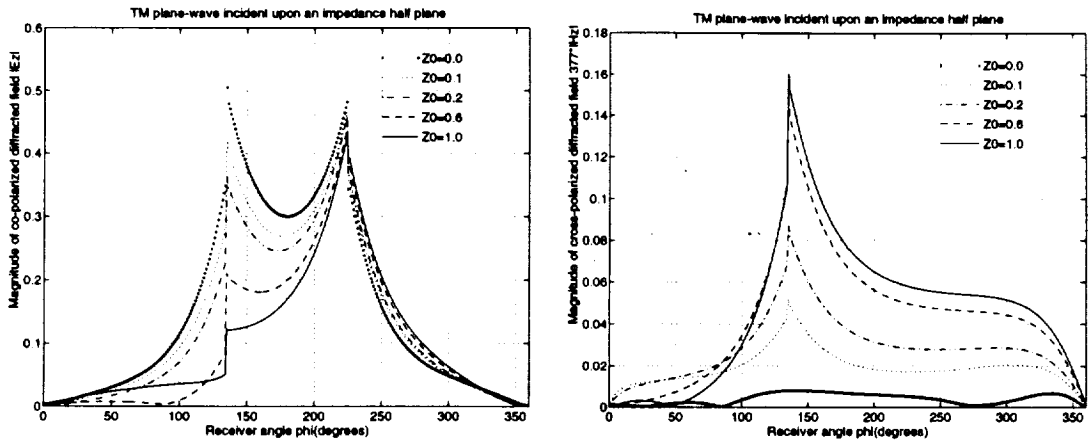

(a) (b)

Figure 4.5: Magnitude of (a) co-polarized E_z^d and (b) cross-polarized $\eta_0 H_z^d$ edge-diffracted fields with E_z^i incident upon an impedance half plane at $\phi_i = 45$ degree as shown in Figure 4.3.

are shown in both figures corresponding to the normalized impedance values $Z_0 = 0, 0.1, 0.2, 0.6$, and 1.0. As the value of Z_0 increases, the co-polarized diffracted field in Figure 4.5(a) shows a significant decrease before it reaches the incident shadow boundary (ISB) at $\phi \approx 225$ degrees. In addition, this field component has the greatest jump at the reflection shadow boundary (RSB) (i.e., $\phi \approx 135$ degrees). The big variations of the diffracted fields at the RSB is due to the dependence of both the reflected and diffracted fields on the surface impedance Z_0. However, this co-polarized field component has little changes around the ISB since the source field is independent of the impedance Z_0. On the other hand, from observing the cross-polarized diffracted field shown in Figure 4.5(b), the diffracted field again has great variations around the RSB, but there is no ISB for this polarization. Note that the increase in the surface impedance value Z_0 gives rises to the cross-polarized diffracted field shown in Figure 4.5(b).

(ii) TE_z Plane-Wave Incident:

This section will investigate the TE_z incident case for the edge diffracted fields. The geometry considered here is similar to the TM_z case, except the incident

field is TE_z polarized, as shown in Figure 4.6. With the field angle fixed at ϕ to 60 degrees, the diffracted field distributions for the cross-polarized and the co-polarized components are separately plotted in Figure 4.7(a) and Figure 4.7(b) as functions of the surface impedance Z_0. According to Figure 4.7(a), the "optimal" impedance is $Z_0 \approx (0.6 + j0.2) * \eta_0\ \Omega$. On the other hand, the cross-polarized diffracted field as shown in Figure 4.7(b) has the strongest magnitude around $Z_0 = 0$, and a minimum at $Z_0 \approx 1.9 * \eta_0\ \Omega$.

Next, the diffracted fields with a TE_z plane-wave incident upon the same impedance half plane as functions of the field angles are studied. The receiver angle ϕ is varied from 0 to 360 degrees, and also the normalized lit-side impedance is chosen to be real and varied between 0 to 1. The cross-polarized and co-polarized diffracted fields are plotted versus the observation angle as shown in Figure 4.8(a) and Figure 4.8(b), respectively. Similar results are obtained for the TE_z-incident case as compared to the TM_z case. According to Figure 4.8(a), the cross-polarized component is only affected by the existence of the RSB which is located at $\phi = 135$ degrees. On the other hand, the co-polarized component shows great variations around the RSB and has little change in magnitude around the ISB as the value Z_0 varies. The same reasons as in the TM_z case can be used to explain these phenomenon.

4.2 Simulated Examples on the NEWAIR3 Code

Following the plane-wave incident cases, this section will emphasize on the results obtained with the NEWAIR3 Code. Seven examples including three ellipsoid-plate geometries are provided for illustrating the new features and flexibilities of the modified NEWAIR3 Code. For each example, the aircraft model is assumed to be operated at the frequency $f = 1GHz$, so one wavelength λ is approximately equal to 1 foot. The aircraft fuselage of each case is assumed to have the same dimensions and is modeled by a PEC composite ellipsoid as illustrated in Figure 4.9. For Examples 1 to 6, the field components are computed around the roll-plane pattern cut as depicted

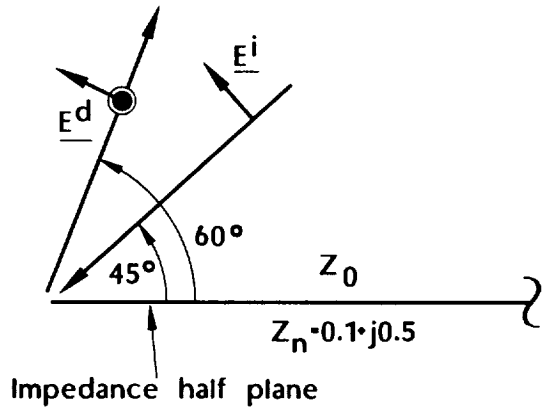

Figure 4.6: Geometry of TE_z plane wave incident upon an impedance coated half plane with a 135-degree diffraction angle measured from the axis of the half plane.

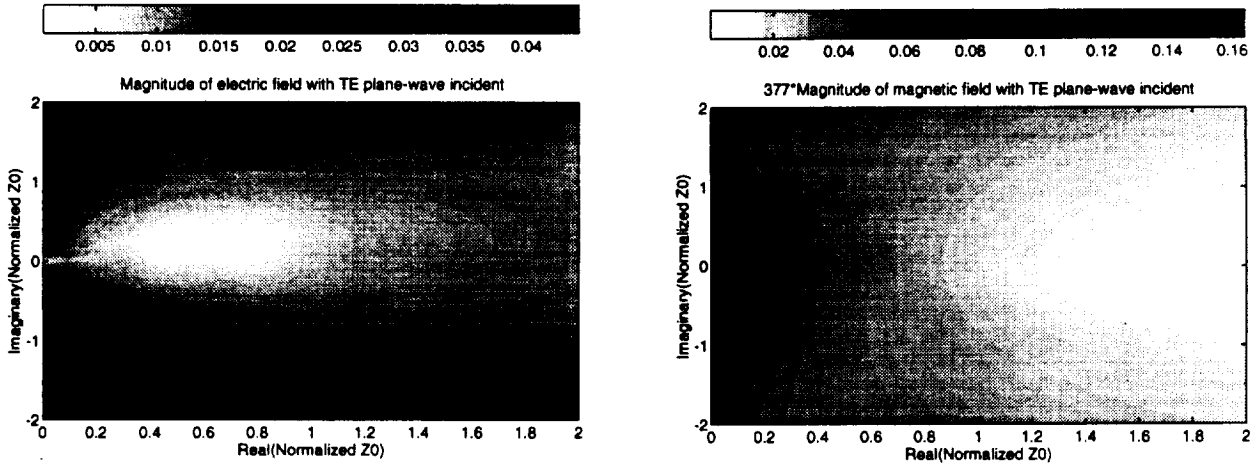

(a) (b)

Figure 4.7: Amplitude distributions of the cross-polarized E_z^d (a) and co-polarized (b) edge-diffracted fields $\eta_0 H_z^d$ with H_z^i incident upon an impedance half plane.

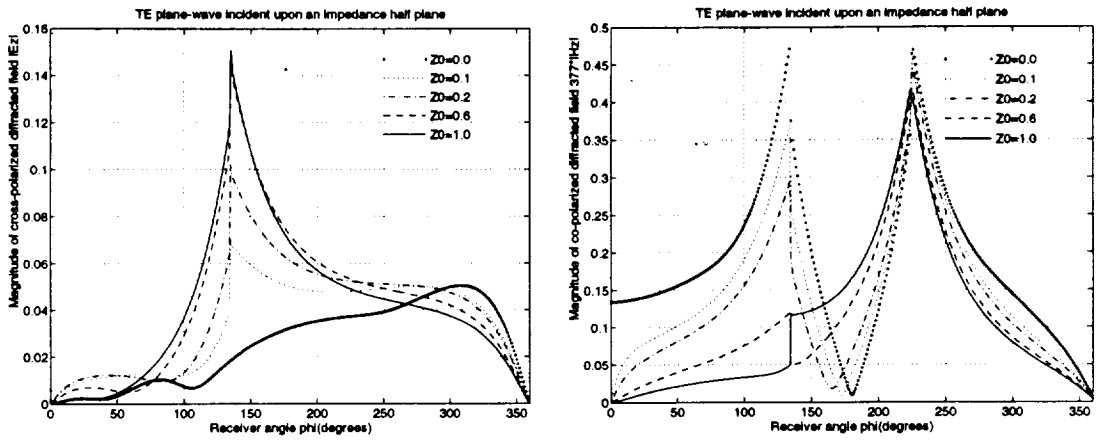

(a) (b)

Figure 4.8: Amplitude distributions of (a) cross-polarized E_z^d and (b) co-polarized $\eta_o H_z^d$ edge-diffracted field with H_z^i incident upon an impedance half plane as shown in Figure 4.6.

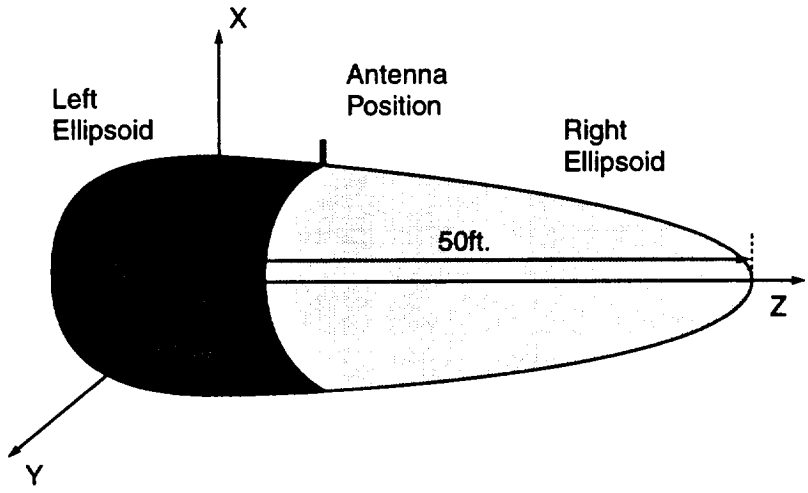

Figure 4.9: Geometry of the aircraft fuselage considered in the NEWAIR3 Code Section.

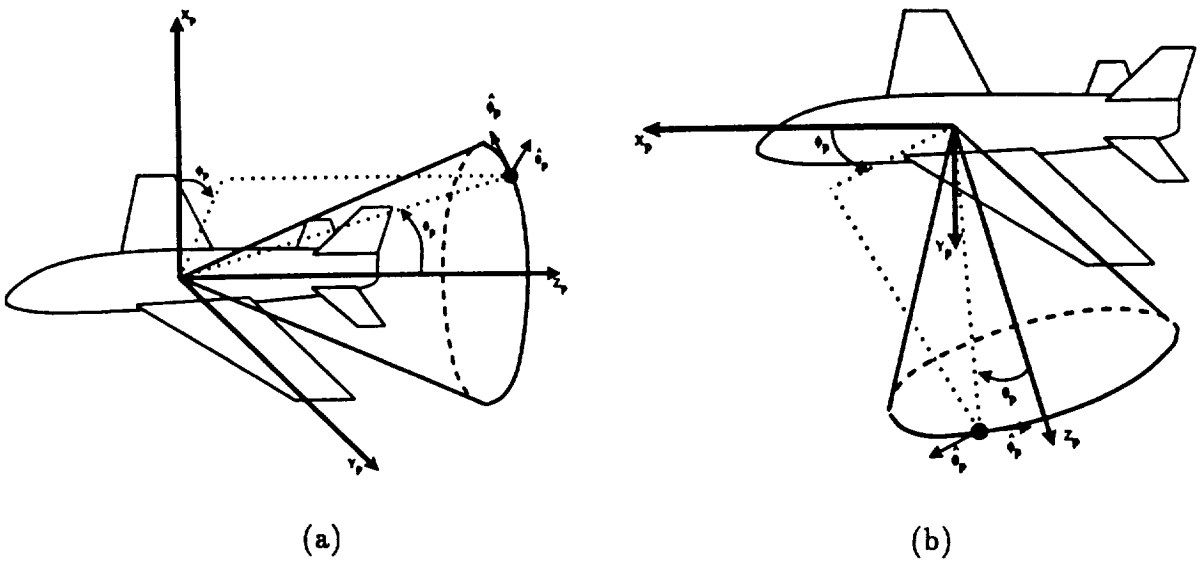

(a) (b)

Figure 4.10: Definitions of the angles θ_p and ϕ_p, and also the unit vectors $\hat{\theta}_p$ and $\hat{\phi}_p$ for (a) the roll-plane and (b) elevation-plane pattern cuts.

in Figure 4.10(a). The angle θ_p is assumed to be 90 degrees and ϕ_p varies from -180 to 180 degrees. The unit vectors $\hat{\theta}_p$ and $\hat{\phi}_p$ are assumed to be in the same directions of the angles θ_p and ϕ_p, respectively. The last example will show the radiated fields computed around the elevation-plane pattern cut as illustrated in Figure 4.10(b) for three different aperture-type antennas. The angle θ_p is assumed to be 80 degrees and ϕ_p is between ± 180 degrees. For more details about the pattern-cut definitions, please refer to the AARP User's Manual [1]. Note that the diffracted fields are assumed to be calculated from all edges of the composite plates, and also all field components are assumed to be normalized with respect to their source field.

4.2.1 Example 1 : Individual first-order field components

Before any comparisons between the results for the composite plates and the PEC plates, the first example of the modified NEWAIR3 Code will assess the validity of the diffraction solutions discussed in Chapter 3. Consider an ellipsoid-plate geometry as illustrated in Figure 4.11. An arbitrary surface impedance with a value of $100+j150\ \Omega$ is assumed on both faces of the plate. The source antenna is assumed to be a quarter-wavelength monopole mounted on the top of the composite ellipsoid. As indicated in Figure 4.11, the incident shadow boundaries ISB1 and ISB2 for the dominant edges

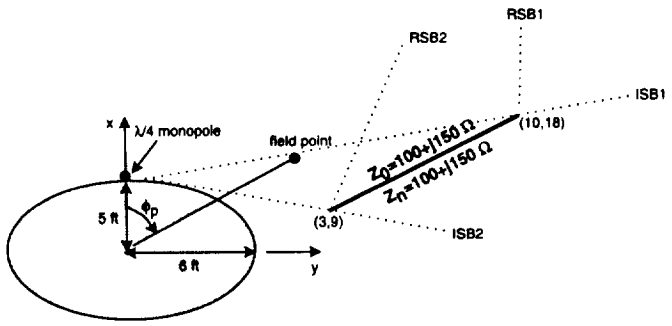

Figure 4.11: Example 1 : The aircraft model consists of a fuselage and a composite plate which is modeled by an impedance plate.

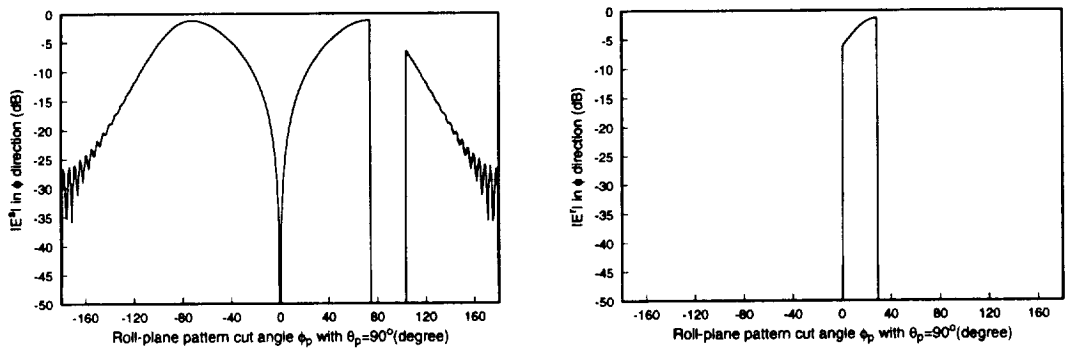

(a) (b)

Figure 4.12: Example 1: Roll-plane radiation patterns for (a) source field and (b) single-reflected field.

are located at $\phi_p = 75^o$ and $\phi_p = 103^o$, respectively. The source field in the region between these two ISBs is expected to be zero. On the other hand, the reflection shadow boundary RSB1 of one of the dominant edges is located at $\phi_p = 36^o$, and one would expect the reflected field to be zero when ϕ_p is greater than 36 degrees. By taking the roll-plane pattern cut of the geometry, the far-zone field patterns are calculated and shown in Figure 4.12(a) to Figure 4.14(b).

As expected, the source field shown in Figure 4.12(a) is discontinuous between $\phi_p \approx 75$ degrees and $\phi_p \approx 104$ degrees, and also the RSB's for the reflected field are located at $\phi_p \approx 36°$ and $0°$ degrees as indicated in Figure 4.12(b). As depicted in Figure 4.13(a), the edge diffracted field has discontinuities at the four shadow boundaries mentioned above and also has a jump around $\phi_p = -120^o$ due to the blockage plates within the composite ellipsoid. If the diffracted field is added to the source field, then

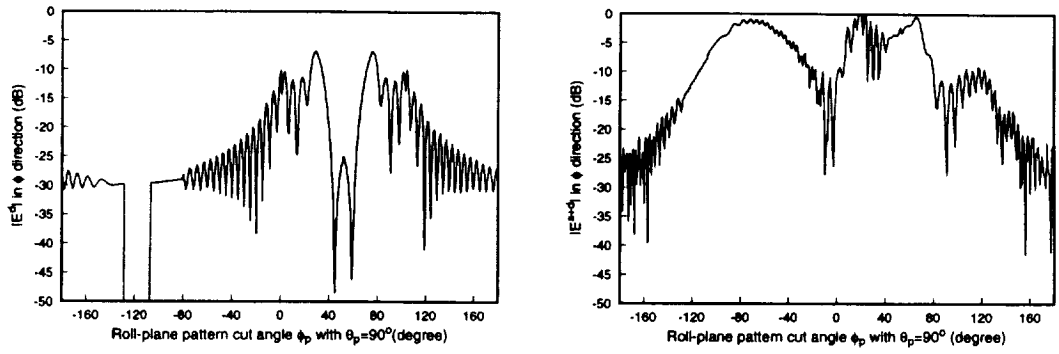

(a) (b)

Figure 4.13: Example 1: Roll-plane radiation patterns for (a) diffracted field and (b) source+diffracted field.

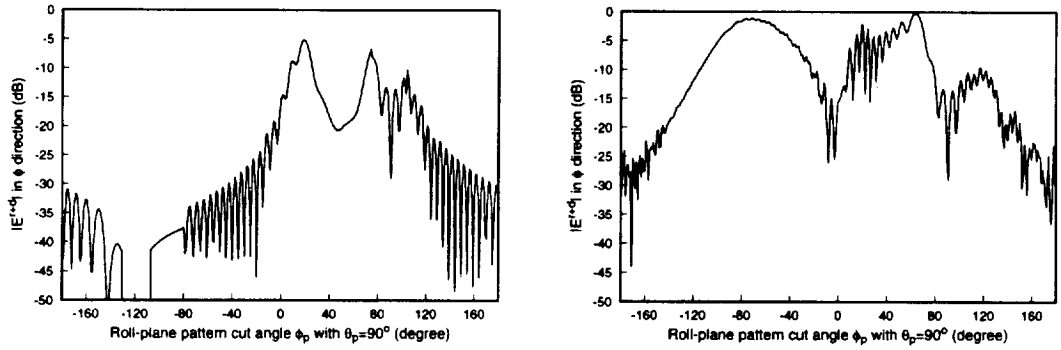

(a) (b)

Figure 4.14: Example 1: Roll-plane radiation pattern for (a) reflected+diffracted field and (b) the 1st order total field.

the summed field in Figure 4.13(b) becomes continuous across the ISB. Similarly, Figure 4.14(a) shows the sum of the reflected and diffracted fields which is continuous across RSB. In addition, the first-order total field as shown in Figure 4.14(b) is continuous everywhere. This also shows that the diffraction solutions for impedance wedges do correct the discontinuities across the GO field shadow boundaries.

4.2.2 Example 2 : Improving the radiation pattern for an aircraft model for $n = 2$ case

This example will emphasize on one of the applications of the composite plates, namely, the reduction of the scattered fields from the plates. By choosing the right impedance values, one can attain a significant improvement of the radiation patterns

around the region where the reflected field exists. The aircraft geometry considered here is the same as the previous example, except a different arbitrary impedance value is assumed for the plate. The lit-side impedance Z_0 is assumed to have the value $226 + j10\ \Omega$, and also the impedance in the shadow face of the plate is $Z_n = 185 + j37\ \Omega$. As shown in Figure 4.16(b), the distortion of the first-order total field caused by the existence of the plate is significantly reduced compared to the result of the one with the PEC plate as depicted in Figure 4.16(a). According to both of the figures, the roll-plane far-zone radiation pattern is plotted against the ideal radiation pattern (i.e., the radiation pattern for which only the fuselage exists) to show the distortions or deviations caused by the plate's existence. By comparing Figure 4.16(a) and Figure 4.16(b), the distortions are reduced by as much as 10 dB in the region where the reflected field exists, i.e., $0 \leq \phi_p \leq 40^o$. Note that the distortion of the ideal pattern behind the impedance plate cannot be fixed because the transmission coefficient of the impedance plate is zero.

4.2.3 Example 3 : Approximate "optimal" impedance value for an aircraft model for $n = 3/2$ case

In this section, the aircraft model with two composite plates which form a right-angle wedge as illustrated in Figure 4.17 is studied. The primary goal of this section is to find an approximate "optimal" impedance value which would reduce the scattered fields. Note that the surface impedance on the lit side of the vertical plate is a PMC which has an infinite surface impedance value. Consider that both plates have the same impedance value denoted as Z, except $Z_0(2) = \infty$. The real part of the impedance is assumed to be between 0 and $\eta_0\ \Omega$. An arbitrary value of 10 is chosen for the imaginary part of the surface impedance. In other words, the values of the surface impedance $Z_0(1)$, $Z_n(1)$, and $Z_n(2)$ are equal to $Re(Z) + j10\ \Omega$, where $Real(Z)$ is chosen to be 10, 150, or 377. Note that the arguments 1 and 2 for the surface impedance Z indicate the plate number.

As illustrated in Figure 4.17, the incident and reflection shadow boundaries of the dominant edge are denoted as ISB and RSB and located at $\phi_p = 107^o$ and $\phi_p = 72^o$,

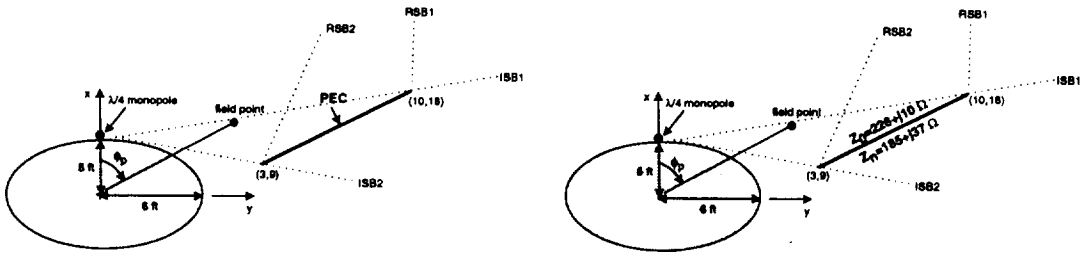

(a) (b)

Figure 4.15: Example 2 : The aircraft models consist of a fuselage and (a) a PEC plate and (b) a composite plate with the source antenna a $\lambda/4$ monopole.

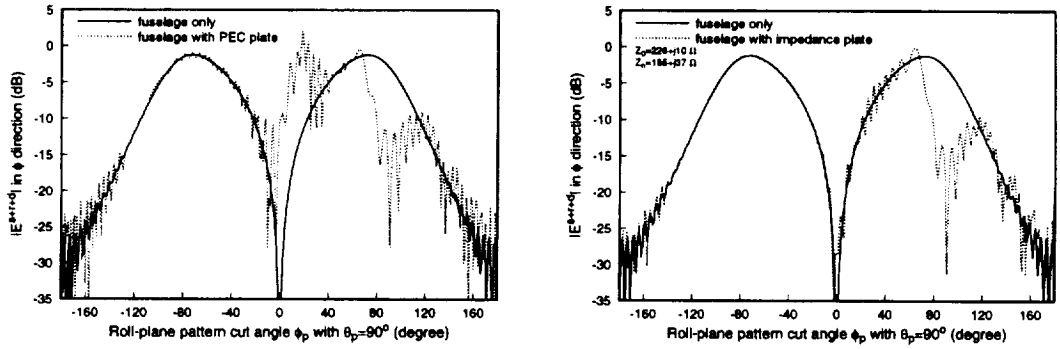

(a) (b)

Figure 4.16: Example 2 : Roll-plane radiation patterns in the presence of (a) the PEC plate and (b) the composite plate.

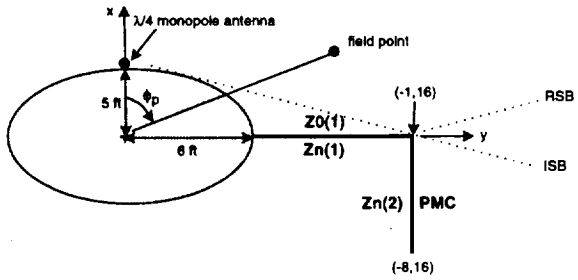

Figure 4.17: Example 3 : An aircraft model consists of a fuselage and two composite plates which are modeled by an impedance right-angled wedge.

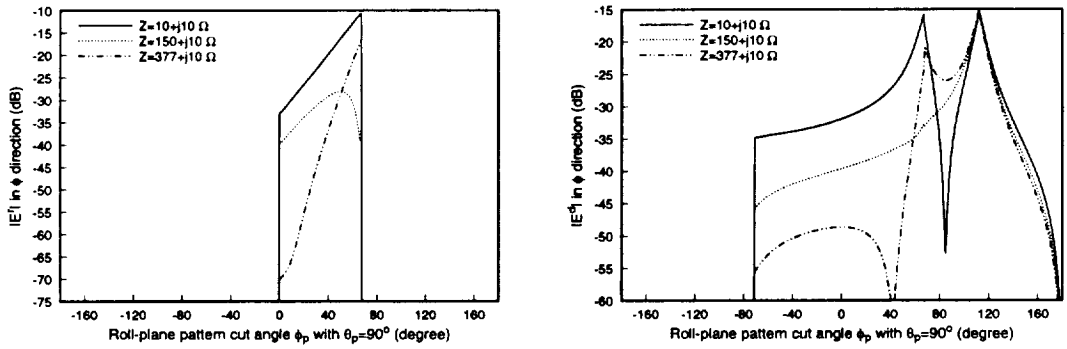

(a) (b)

Figure 4.18: Example 3 : Roll-plane radiation patterns for (a) the single-reflected field and (b) the diffracted field.

respectively. Figure 4.18(a) and Figure 4.18(b) show the reflected fields and diffracted fields for $Re(Z) = 10, 150$, and 377. Note that there is a significant change around the RSB ($\phi_p \approx 75^o$) and a little change around ISB for the diffracted field. For the impedance $Z = 150 + j10\ \Omega$, the overall reflected field is below -25 dB. When $Re(Z)$ is increased to 377, the reflected field is fairly small until the pattern-cut angle ϕ_p exceeds 50 degrees. In addition, the diffracted field corresponding to the one with $Z = 150 + j10\ \Omega$ has the lowest value around the RSB. Thus, the surface impedance $Z = 150 + j10\ \Omega$, which will be referred as the "optimal" impedance value for this case, is the best choice over the other two to minimize the scattered fields.

4.2.4 Example 4 : Improving the radiation pattern for an aircraft model for $n = 3/2$ case

In this example, the "optimal" surface impedance $Z = 150 + j10\ \Omega$ obtained from the previous section is simulated in the NEWAIR3 Code, and also compared to the one with PEC plates. It is expected that the composite-plate model will significantly improve the radiation pattern around the region where the reflected field exists (i.e., $0 \leq \phi_p \leq 75^o$). By comparing the dotted lines in Figure 4.20(b) and Figure 4.20(a), the radiation pattern for the impedance plate model is much closer to the "ideal" quarter-wavelength monopole pattern as shown in the solid lines in both figures. This improvement is due to the fact that the surface impedance on the plates has eliminated the undesired scattered fields by as much as 5 dB around the region where ϕ_P is between 10 to 75 degrees.

4.2.5 Example 5 : Approximate "optimal" impedance value for an aircraft model with two composite plates for $n = 1$ case

In this section, a two-part impedance plate as depicted in Figure 4.21 is considered. Assume both plates have the same surface impedance values with the imaginary part of the impedance fixed to 10. Note that this case was run to test the solution for $n = 1$. It is obvious that this example also corresponds to the $n = 2$ case since the impedance values on both sides of the junction are the same. In order to find

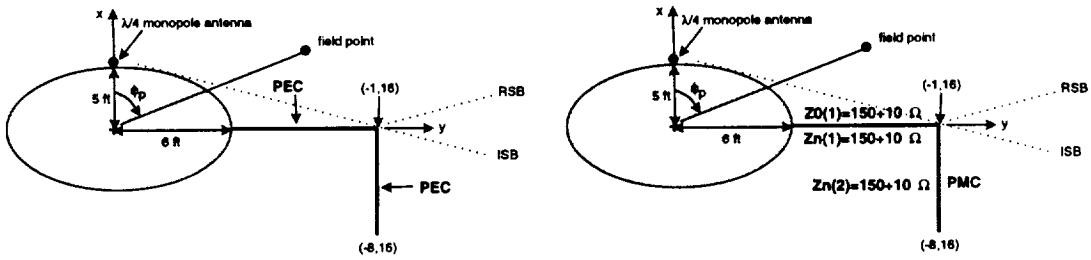

Figure 4.19: Example 4 : An aircraft model consists of a fuselage and two composite plates which are modeled by (a) the PEC plates or (b) the impedance plates with a $\lambda/4$ monopole as the source antenna.

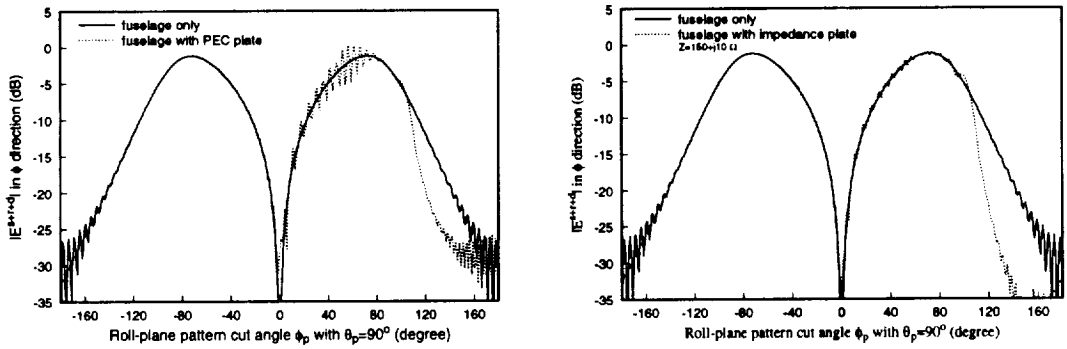

Figure 4.20: Example 4 : Roll-plane radiation patterns for simulating an aircraft model with (a) the PEC plates and (b) the composite plates.

the "optimal" surface impedance for this geometry, the real part of the impedance is chosen to be 10, 150, or 377 for the purpose of minimizing the scattered fields from the plates. According to the aircraft geometry as depicted in Figure 4.21, the reflection shadow boundaries RSB1 and RSB2 for the dominant edges are located at $\phi_p = 80$ degrees and $\phi_p = 50$ degrees, respectively. The reflected field is expected to exist in the region between RSB1 and RSB2 (i.e., $50° \leq \phi_p \leq 80°$). In addition, the incident shadow boundaries ISB1 and ISB2 for the dominant edges are located at $\phi_p = 100$ degrees and $\phi_p = 129$ degrees, respectively. The source field is expected to be zero in the region between ISB1 and ISB2. Moreover, the diffracted field is expected to have the greatest variations around the various shadow boundaries.

The far-zone reflected and diffracted fields are computed around the roll-plane pattern cut and depicted in Figure 4.22(a) and Figure 4.22(b), respectively. The reflected field corresponding to the impedance value $Z = 150 + j10\ \Omega$ has the lowest magnitude as illustrated in Figure 4.22(a). In addition, according to Figure 4.22(b), the diffracted field corresponding to the one with $Z = 150 + j10\ \Omega$ has the lowest distribution around the RSB. Thus, $Real(Z) = 150$ is the best choice among the three impedance values considered here. Note that the zero values of the diffracted fields between $-100°$ and $-80°$ is due to the blocking plates being used in this example.

4.2.6 Example 6 : Improvements of the radiation pattern for an aircraft model (with two composite plates) for $n = 1$ case

This section will implement the "optimal" impedance value $Z = 150 + j10\ \Omega$ obtained from the previous example, and also compare with the result for the PEC plates. Note that the radiation pattern shown in Figure 4.24(b) is almost identical to the "ideal" monopole radiation shown in the solid line for most of the regions. By comparing this figure with the one shown in Figure 4.24)(a), the scattered fields have been reduced as much as 8 dB around the region where RSB1 and RSB2 are located.

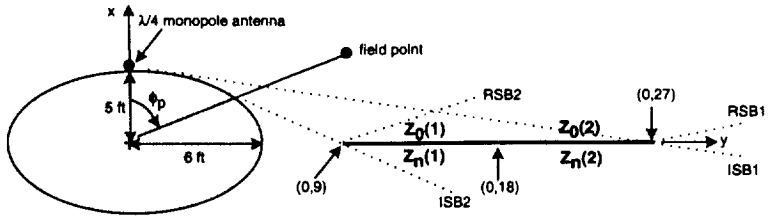

Figure 4.21: Example 5 : An aircraft model consists of a fuselage and two composite plates which are modeled by a two-part impedance plane.

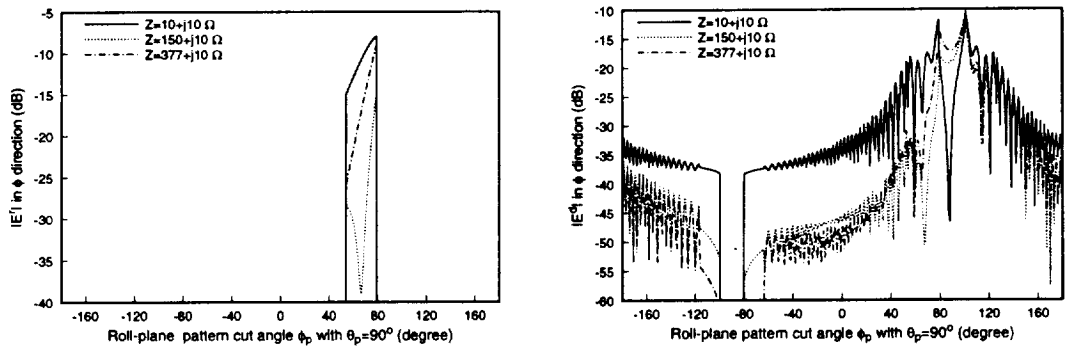

(a) (b)

Figure 4.22: Example 5 : Roll-plane radiation patterns for (a) the single-reflected field and (b) the diffracted field.

4.2.7 Example 7 : Radiation patterns for aperture-type antennas

In this example, the same geometry as in Section 4.2.1 is considered, and the primary goal here is to investigate the radiation patterns for various aperture-type antennas. The aircraft geometry with an antenna source mounted on the top of the composite ellipsoid is depicted in Figure 4.25. Three types of antennas are studied here: an axial slot, a circumferential slot, and a rectangular microstrip patch antenna. The microstrip antenna is included here because its radiation pattern can be calculated by modeling the patch by slots located around its edge. The impedance values are arbitrarily chosen as $Z_0 = 100 + j100\ \Omega$ and $Z_n = 200 + j200\ \Omega$. The far-zone first-order total fields are computed in the elevation plane with θ_p[4]=80 degrees.

[4]Please refer to Figure 4.9 and the AARP User's Manual [1] for more details on the pattern-cut definitions.

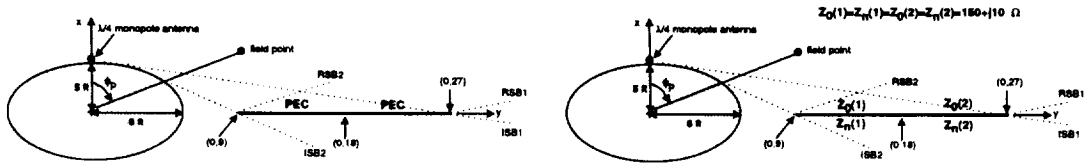

Figure 4.23: Example 6 : An aircraft model consists of a fuselage and (a) two PEC plates or (b) two composite plates which are modeled by a two-part impedance plane.

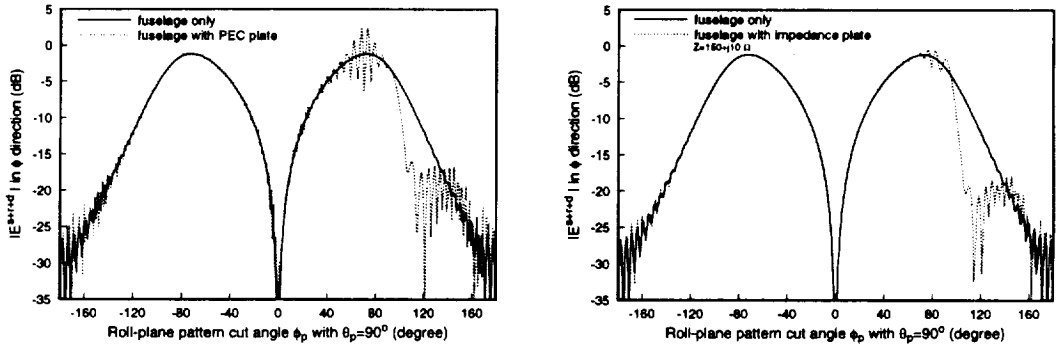

Figure 4.24: Example 6 : Roll-plane radiation patterns for simulating an aircraft model with (a) PEC plates and (b) impedance plates.

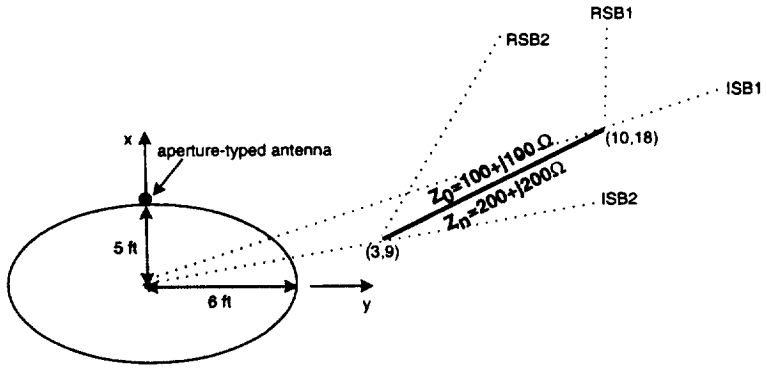

Figure 4.25: Example 7 : An aircraft geometry of a fuselage with a composite plate where an antenna source is mounted on top of the fuselage.

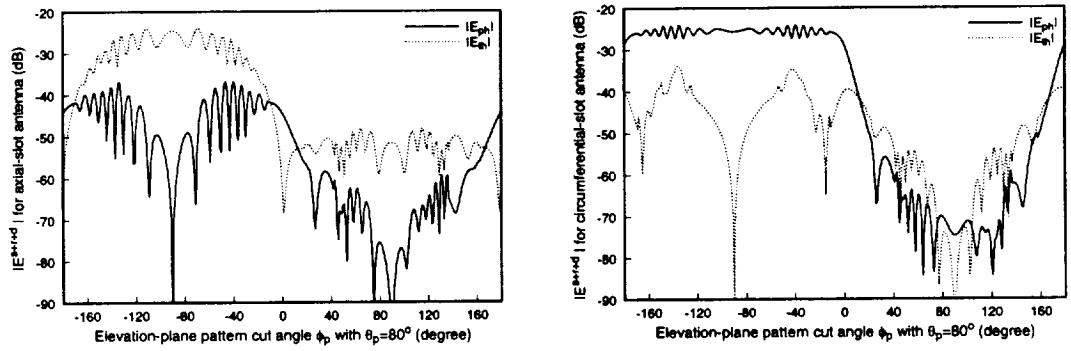

(a) (b)

Figure 4.26: Example 7 : Elevation-plane radiation patterns of aircraft model with (a) an axial-slot antenna source and (b) a circumferential-slot antenna source mounted on top of the composite ellipsoid.

First, an axial slot (ref. to Figure 2.2(a)) is placed on top of the fuselage. Since the long dimension of the slot is along the length of the fuselage, the electric field radiated by the slot is then polarized in the $\hat{\theta}_p$ direction as shown in Figure 4.10(b). As a result, the θ_p component of the electric field should be dominant compared to the ϕ_p component. As shown in Figure 4.26(a), the magnitude of the electric field $|E_{th}|$ which is in the $\hat{\theta}_p$ direction generally dominates the ϕ_p component (i.e., $|E_{ph}|$) in the lit region.

Next, an circumferential slot (ref. to Figure 2.2(b)) as the antenna source is considered. Since the orientation of the source in this case is orthogonal to the previous case (i.e., the axial slot antenna), the dominant field is expected to be in the $\hat{\phi}_p$ direction in this case. As shown in Figure 4.26(b), $|E_{ph}|$ in general is at least 10 dB higher than $|E_{th}|$ in the lit region.

Finally, a rectangular microstrip patch is considered as the antenna source mounted on top of the fuselage. The model used here assumes that this antenna is radiating its dominant mode. The microstrip antenna is oriented in the way such that the angle BETADA= 60 degrees and the dimensions $SLOTBB$ and $SLOTAA$ are 0.5λ and 0.6λ[5], respectively. The field patterns are expected to be the combination of the results from both the axial and circumferential slots. The radiation patterns in $\hat{\theta}_p$ and $\hat{\phi}_p$ directions are depicted in Figure 4.28. The magnitude of both field components are relatively large. The θ_p field component has a similar pattern shape as the ϕ_p component of the axial-slot example, and also $|E_{ph}|$ is similar to $|E_{ph}|$ of the circumferential slot, except that the magnitude is approximately 35 dB higher! This last example ends the discussions of numerical results. In the following chapter, a conclusion will summarize this report.

[5]Please refer to Figure 4.27 and Appendix A for the definition of the angle BETADA.

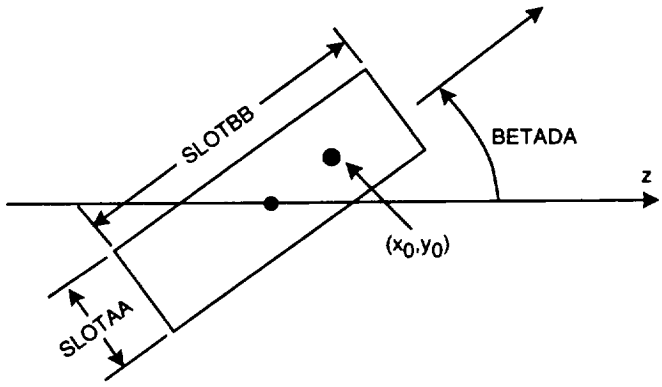

Figure 4.27: Definitions of dimensions SLOTAA and SLOTBB and angle BETADA. Note that SLOTBB is the resonant length.

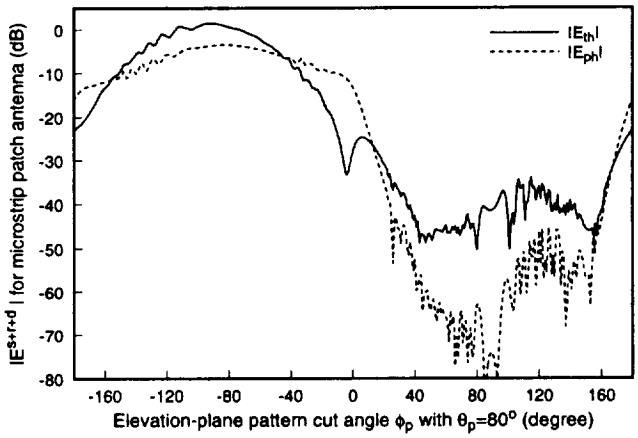

Figure 4.28: Example 7 : Elevation-plane radiation pattern of aircraft model with a rectangular microstrip-patch antenna source mounted on top of the composite ellipsoid.

Chapter 5

Summary and Conclusions

In this report, the UTD-based NEWAIR3 Code has been modified such that it has the capability to model modern aircraft constructed in part by conductor-backed composite materials. One good model of conductor-backed composites is the impedance boundary condition where the composites are replaced by surfaces with complex impedances. In most applications, the aircraft distorts the desired pattern of the antenna. Thus, the test examples for the modified NEWAIR3 Code mainly emphasize reducing the undesired scattered fields from the surface impedance plates. The following three sections summarize the report, describe the main contributions of the report, and finally suggest areas for future study.

5.1 Summary

The list below shows the steps followed to modify the NEWAIR3 Code to add the capability of modeling composite flat plates by impedance plates.

(i) obtain the source-field solutions, including the solutions for monopoles and slots which are described in [2] and the results for the microstrip antennas which are obtained from [12],

(ii) develop Fresnel reflection coefficients for which the total field consisting of an incident plane wave and the reflected field satisfies the impedance boundary at the surface of the plate,

(iii) obtain the plane-wave incident solutions for the edge diffracted fields which are described in [10] and summarized in Chapter 3 and Appendix B, and

(iv) modify both the solutions from Step ii and Step iii for spherical illuminations such that the modified solutions are compatible with the NEWAIR3 Code.

All the steps mentioned above are discussed and presented in Chapter 2 and Chapter 3. Chapter 4 shows numerical results for plane-wave cases and for the NEWAIR3 Code cases:

(i) the plane-wave cases,

  (a) study the reflected and diffracted fields as a function of the surface impedances, and

  (b) study the diffracted field as a function of the observation angles.

(ii) the NEWAIR3 Code cases,

  (a) assess the validity of the diffraction solutions obtained from Chapter 3,

  (b) improve the on-aircraft antenna radiation patterns for three ellipsoid-plate models, and

  (c) illustrate that the rectangular microstrip patch antenna can be modeled by a pair of slot antennas available in the modified NEWAIR3 Code.

5.2 Report Contributions

The current study has made the following contributions:

(i) modified the NEWAIR3 Code by adding the capability of modeling composite flat plates by impedance plates,

(ii) developed new Fresnel dyadic reflection coefficient for impedance surfaces,

(iii) modified the polarization transformation matrix, i.e., [T] matrix, such that it is able to transform incident fields at a receiver's image location into reflected fields (from impedance plates) at the receiver location.

(iv) added the rectangular microstrip patch antenna as one of the aperture-type antennas available in the NEWAIR3 Code, and

(v) revised the NEWAIR3 Code into independent subroutines and organized similar computations into one subroutine to enhance the computational efficiency (see Appendix A).

5.3 Further Research Direction

Accurate electromagnetic diffraction solutions are not available for other wedge angles besides the four special cases mentioned in Chapter 3. For more practical applications, the development of general diffraction solutions for an impedance wedge with an arbitrary wedge angle is necessary. In addition, the solution for the corner diffracted fields are also under investigations and it is necessary for finite-sized material plates. Finally, replacing the PEC ellipsoid by an ellipsoid whose surface is modeled by a complex impedance is necessary to complete the conductor-backed composite models for the NEWAIR3 Code. This is being pursued at the ElectroScience Laboratory.

Appendix A

Summary of the Modifications on Newair3 Code

The Newair3 Code is a Fortran 77 computer code which was developed to simulate the radiation patterns of antennas mounted on a composite ellipsoid and in the presence of a finite set of flat PEC plates. In order to reduce the effect of the plate structures on the antenna radiation patterns, the code was modified so it can now handle material-coated metal plates which are modeled by impedance surfaces. Thus, new subroutines for computing the reflection and diffraction coefficients for impedance surfaces and wedges are implemented in the original NEWAIR3 Code. Furthermore, besides monopole and slot antennas, rectangular microstrip-patch antennas are also available as radiation sources for the aircraft code. Note that the radiated source's pattern factors are reorganized in two separated subroutines. It is worth mentioning that all additions and modifications to the Newair3 Code for the current research are followed by the initials shk.

A.1 Modifications to Input-Data Command

Some modifications on the input-data commands, which are defined in the main program, are made to provide more flexibility to the NEWAIR3 Code. First, for the plate-geometry related command **PG**, the material of a plate can be selected after the plate's coordinates are defined. If the **MATERIAL(MPX)** is selected to be "one", then the plate is a perfectly electrical-conducting plate. On the other hand, if

"two" is defined for a plate's material, then one has to enter the real and imaginary parts of the complex impedance values Z_0 and Z_n for both faces of the plate. Note that the surface impedance on the lit side of a plate (i.e., Z_0) is first entered to the input data, and then followed by the surface impedance on the shadow side of the plate (i.e., Z_n). The following shows the modified input format for the **PG** command and please refer to [1] for more descriptions on the original input variables.

```
PG:
MCX(MPX), LATACH(MPX)
(PVC(N,ME,MPX), N=1,3)
MATERIAL(MPX)
REAL(Z0), IMAG(Z0), REAL(Zn), IMAG(Zn)
```

There are two ways to define a PEC plate:

1. Set the **MATERIAL(MPX)** to one and ignore the following read variables.
2. Set the **MATERIAL(MPX)** to two and define all real and imaginary parts of Z_0 and Z_n to be zero.

One example to define an impedance plate would be:

```
PG: Z0=377.+j10 Ω and Zn=0+j150 Ω
4, F
4., 14., -20.
6., 14., -20.
6., 14., 20.
4., 14., 20.
2
377., 10., 0., 150.
```

Also, the plate surface is considered to be a PEC if the absolute value of a given impedance value is less than 0.001. In addition, the surface of a plate is considered to be a PMC if its absolute impedance value is greater than 10^6.

Next, the input command **SG** is also modified to make a rectangular microstrip-patch antenna [13] available in the NEWAIR3 Code. Assuming that the antenna is operating at or near the lowest-order resonant frequency TM_{10} as described in [13], then the microstrip patch can be replaced by two magnetic dipoles. Since the aircraft code already models a slot antenna by a magnetic dipole [2, 1], the two magnetic dipoles can be easily implemented. The major difference between the two magnetic dipoles used to model the microstrip antenna and the existing ones in the NEWAIR3 Code is that the fields in the latter ones have a cosine distribution along their long dimensions, but the currents on the "new" magnetic dipoles are constant. The following gives the modified **SG** input format for rectangular microstrip antennas.

SG:
PHS, ZS
MSX
RHOA(MS), PHIA(MS)
SLOTAA(MS), SLOTBB(MS), BETADA(MS), SMONOA(MS), JANTA(MS)
WMA(MS), WPA(MS)
TSE, X0, Y0, CER,CERI

The parameter **JANTA(MS)** defines the type of antennas as follows:

```
                1 -> SLOT ANTENNA (AXIAL OR CIRCUMFERENTIAL),
JANTA(MS)   =   2 -> MICROSTRIP PATCH ANTENNA,
                3 -> RADIAL MONOPOLE ANTENNA.
```

When a slot or a monopole antenna is chosen as the radiation source in the aircraft code, the last line of the inputs for **SG** are ignored and should not be used. On the other hand, if **JANTA(MS)**=2, **SLOTAA(MS)** and **SLOTBB(MS)** denote the nonresonant and resonant lengths of the microstrip patch antenna (see Figure A.1). In addition, the parameter **BETADA(MS)** represents the angle between the axis of the fuselage (i.e., $\hat{z}$ direction) and the microstrip antenna and is measured in the counter-clockwise direction as shown in Figure 4.27. The parameter **TSE** represents

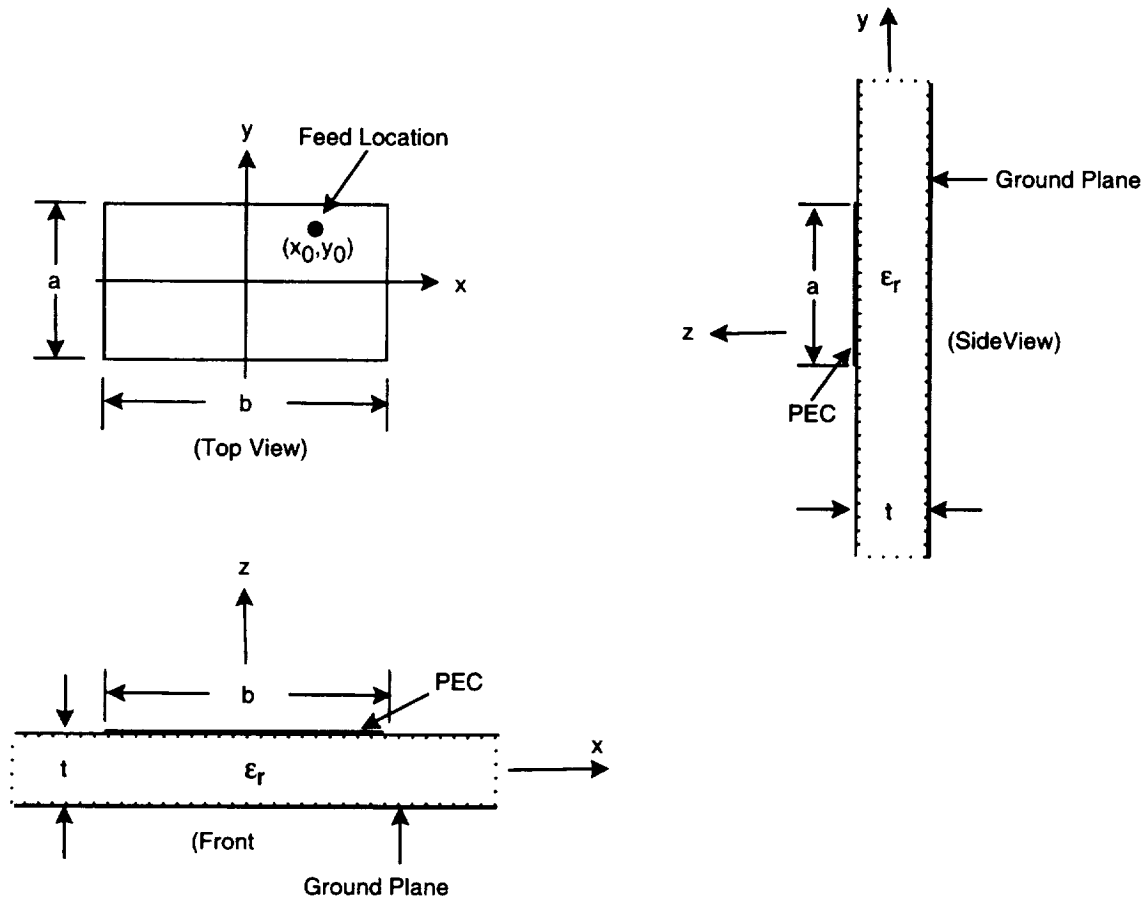

Figure A.1: The geometry of a rectangular microstrip antenna.

the thickness of the substrate of a microstrip antenna, (X0,Y0) are the coordinates of the feed point, and **CER** and **CERI** are the real and imaginary parts of the relative dielectric constant ϵ_r. For more details about the microstrip antenna in the aircraft code, please refer to [13].

The following shows an example of defining a rectangular microstrip patch antenna as a radiation source in the NEWAIR Code:

```
SG: RECTANGULAR MICROSTRIP PATCH
0.0, 0.1
1
0.0, 0.0
0.14, 0.28, 60.0, 0.0845, 2
1.0, 0.0
0.05, 0.1, 0.0, 4.0, 0.0
```

A.2 Additions/Modifications on Programs

The following documents the new subroutines and modifications on the original subroutines of the NEWAIR3 Code.

1. Subroutine CMATRIX – This subroutine calculates the elements of the transformation matrix $\bar{\bar{S}}$. By multiplying this matrix to the incident field, the "normal" incident field with respect to the wedge walls is obtained. After the edge diffraction is computed, the inverse of the transformation matrix can be multiplied by the diffraction coefficient and the "normal" incident field to obtain the tangential diffracted field. For more details on CMATRIX, please refer to Chapter 3 where the discussions on the transformation matrix are detailed.

2. Subroutine CONSTANT1 – This subroutine computes the constant matrices $\bar{\bar{B}}_1$ and $\bar{\bar{D}}_1$ for the edge diffraction with the wedge number n equals to one. The expressions are given in (B.4) and are obtained from the equation (B.2).

3. Subroutine CONSTANT2 – This subroutine calculates the same constant matrices as CONSTANT1, except that this subroutine is used for impedance half planes. Please refer to (B.6) for the $\bar{\bar{B}}_2$ and $\bar{\bar{D}}_2$ expressions .

4. Subroutine CONSTANT3 – The $\bar{\bar{B}}$ and $\bar{\bar{D}}$ (see (B.10)) for impedance right-angle wedges are computed in this subroutine. All these constant matrices are solved from Equation (B.2) (i.e., for the purpose of removing the poles due to the inverse of $\bar{\bar{S}}$). Please refer to Chapter 3 for more details.

5. Subroutine DIFF_COEF – This subroutine computes the elements of a 2 by 2 dyadic diffraction coefficient (refer (3.24)) for diffraction at an impedance wedge. All equations are referenced from [10] and are discussed in Chapter 3. Numerical results have been shown that by taking the limits on the impedance values to zero, the modified code has almost identical results as compared to the original NEWAIR3 Code.

6. Subroutine DIFFLD – The modifications on this subroutine are for the purpose of making impedance plates available in addition to PEC plates for the NEWAIR3 Code. Depending on the selected plate's material, this subroutine decides to call either the original diffraction coefficient subroutine WD or the the new DIFF_COEF subroutine. If the **MATERIAL(MPX)** for the MPX^{th} plate is chosen to be "2", then the DIFFLD subroutine starts to look for the correct impedance values for a wedge formed by the MPX^{th} plate with the other structure of an aircraft. Here we consider three cases to form a wedge.

   (i) A single plate (i.e., the plate is not attached to any obstacle): This case is considered to be an impedance half plane. The impedance values Z_0 and Z_n are entered in the given order at the last line of the input data in the PG command.

   (ii) A plate is attached to another plate: Z_0 is the impedance value on the lit side of the MPX^{th} plate. Z_n is the lit-side impedance of the plate attached to the MPX^{th} plate.

(iii) A plate attached to the perfectly electrical-conducting fuselage: Since we only have solutions for right-angled wedges, half planes, and two-part impedance planes, the plate has to be attached to the fuselage at the center line [1]. Thus, Z_0 is the lit-side impedance value of the attached plate and Z_n is zero since the fuselage is a PEC.

After the appropriate impedance values are selected, the DIFFLD subroutine computes the diffraction coefficient and then the diffracted field for each plate with a desired pattern cut.

7. Subroutine DTMATRIX – This subroutine computes the elements of the matrix that maps the incident field at the receiver's image location (after double reflection) into the reflected field at the receiver location. In this subroutine, the T_MATRIX is called twice so that the incident field is transformed into a reflected field after reflection from the first plate and subsequently after reflection from the second plate. A call statement of DTMATRIX is added to the RRFLD subroutine for calculating double-reflected fields from all the plate structures.

8. Subroutine MMATRIX – The expression for the elements of $\bar{\bar{M}}$ is given in (3.19) and this matrix is related to the Maliuzhinets functions by (3.18). Limits are taken as the impedance approaches to zero and infinity, and they are summarized in Table 3.3. This subroutine is used in the computations of the edge diffraction.

9. Subroutine MATLIB – This is a math library which contains various math operations on complex matrices.

10. Subroutine PATFACT_SOURCE – The purpose of adding this subroutine is to organize all the pattern-factor expressions for various antenna sources into a single subroutine. This subroutine is been called by the following three subroutines: ELLFLD, DIFINC, and DINLIT.

[1] Refer to the Airborne Antenna Radiation Pattern USER'S MANUAL [1] for more details about the attachment to an aircraft fuselage.

11. Subroutine REFL_COEF – The parallel and perpendicular reflection coefficients are computed in this subroutine. Limits on the coefficients have been taken for the perfectly electrical-conducting case. This subroutine is called in T_MATRIX.

12. Subroutine THIMATRIX – This subroutine involves the computations of products of well-known Maliuzhinets functions. The expressions of the 2 by 2 matrix is given in (3.16) and some limits as the impedance approaches zero or infinity are taken and summarized in Table 3.1 and Table 3.2. For more details, please see Chapter 3.

13. Subroutine T_MATRIX – This subroutine is added to replace the original REFGEO subroutine. T_MATRIX (refer (2.34)) maps the incident field at the receiver's image position into the reflected field at the receiver location. This matrix is called in the subroutine REFFLD.

Note that the original Newair3 Code has been broken down into a main program and subroutines which are contained in the same-named files. A GNU makefile is also written to include all programs involved the NEWAIR3 Code to shorten the compilation time.

Appendix B

The Constants $\bar{\bar{B}}_n$ and $\bar{\bar{D}}_n$

The 2×2 matrices $\bar{\bar{B}}_n$ and $\bar{\bar{D}}_n$ are included in the expression of diffraction coefficient (3.9) to eliminate the singularities introduced by the inverse of the transformation matrix $\bar{\bar{S}}(\alpha)$. To satisfy the edge condition for the spectral function in (3.5),

$$\lim_{|Im(\alpha)|\to\infty} \bar{F}_z(\alpha) = \text{constant vector}, \tag{B.1}$$

the constant matrices $\bar{\bar{B}}_n$ and $\bar{\bar{D}}_n$ can then be obtained by solving the following equation:

$$\begin{aligned} \underline{v}^{\pm} \cdot \bar{\bar{\Psi}} \quad & \left\{ \frac{\bar{\bar{I}}}{\sigma_n(\alpha) - \sigma_n(\frac{n\pi}{2} - \phi')} + \bar{\bar{B}}_n + \bar{\bar{D}}_n \, sin(\frac{\alpha_k^{\pm}}{n}) \right\} \\ & \cdot \bar{\bar{\Psi}}^{-1} (\frac{n\pi}{2} - \phi') \, \bar{\bar{S}} \, (\frac{n\pi}{2} - \phi') \bar{F}_{oz} = 0. \end{aligned} \tag{B.2}$$

The $\alpha_k^{\pm}$ are the poles of $\bar{\bar{S}}^{-1}$ depicted in Figure B.1 for each special case and

$$\begin{aligned} & \sigma_n(\alpha) = sin(\frac{\alpha}{n}), \\ & \underline{v}^{\pm} = \begin{bmatrix} \pm j & 1 \end{bmatrix}, \\ & \text{and} \\ & \bar{F}_{oz} = \begin{bmatrix} E_{0z} \\ \eta_0 H_{0z} \end{bmatrix}, \end{aligned} \tag{B.3}$$

where E_{0z} and H_{0z} are arbitrary constants for incident electric and magnetic fields, respectively, and η_0 is the intrinsic impedance in free-space. Note that $\underline{v}^{\pm}$ is a 1×2 row vector.

In the following, the expressions for $\bar{\bar{B}}_n$ and $\bar{\bar{D}}_n$ are presented (see details in [14, 15]).

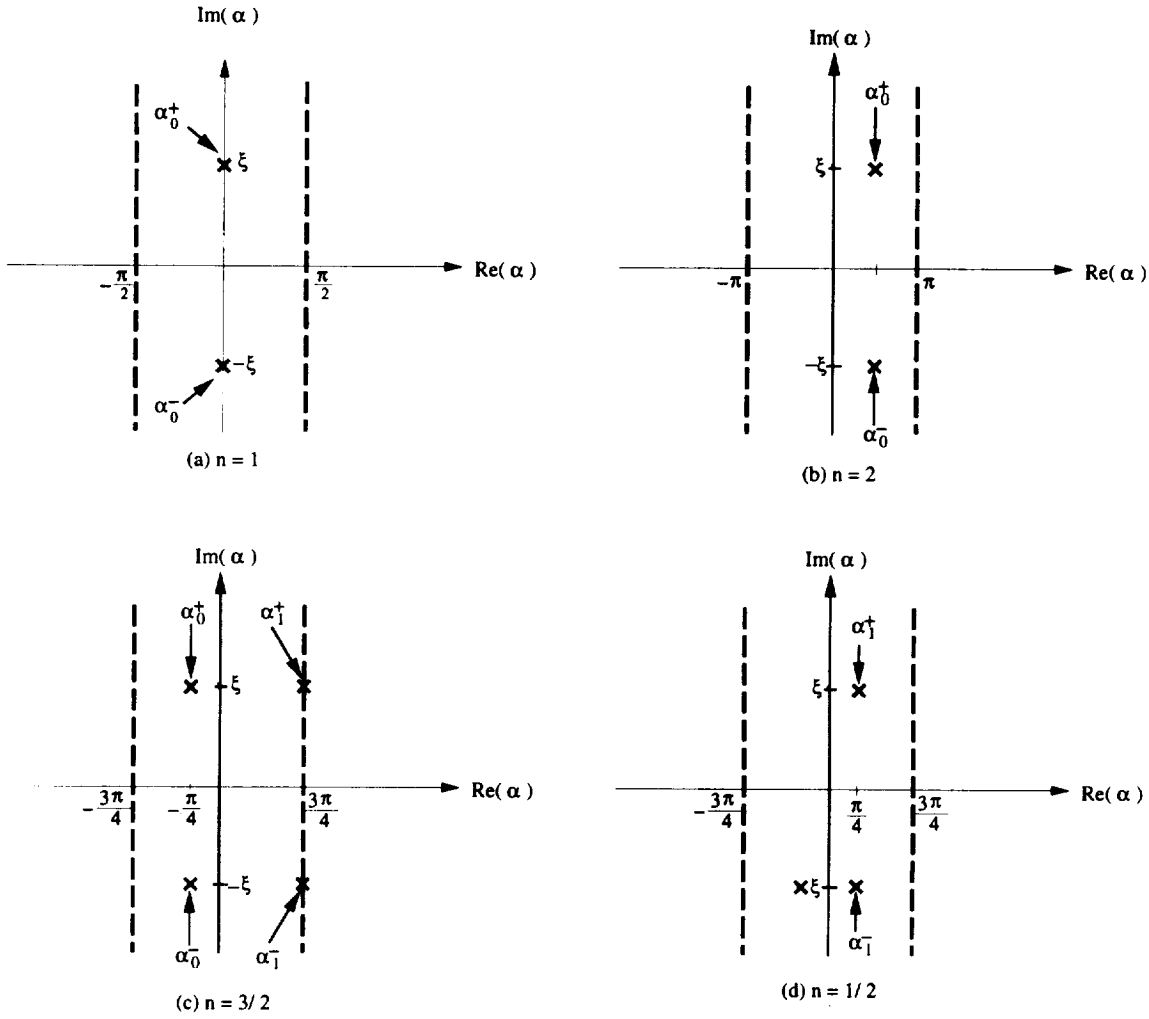

Figure B.1: The poles of $\overline{\overline{S}}^{-1}(\alpha)$ for: (a) n = 1, (b) n = 2, (c) n = $\frac{3}{2}$, and (d) n = $\frac{1}{2}$.

(i) n = 1:

$$\bar{\bar{B}}_1 = -\bar{\bar{N}}_1^{-1}(\alpha_0^+)\,\bar{\bar{Z}}_1^{-1}(\alpha_0^+)\,\bar{\bar{N}}_1(\alpha_0^+),$$

$$\bar{\bar{D}}_1 = \begin{bmatrix} 0 & 0 \\ 0 & 0 \end{bmatrix}, \tag{B.4}$$

in which the poles $\alpha_0^{\pm} = \pm j\xi$ and $\xi = ln(\frac{(1-cos\beta)}{sin\beta})$. The functions $\bar{\bar{Z}}_n(\alpha)$ and $\bar{\bar{N}}_n$ can be written as

$$\bar{\bar{Z}}_n(\alpha) = \sigma_n(\alpha)\,\bar{\bar{L}} - \sigma_n(n\pi/2 - \phi')\,\bar{\bar{I}},$$

$$\bar{\bar{N}}_n(\alpha) = \begin{bmatrix} \underline{v}^+\,\bar{\bar{\Psi}}(\alpha) \\ \underline{v}^-\,\bar{\bar{\Psi}}(-\alpha) \end{bmatrix}, \tag{B.5}$$

where $\bar{\bar{L}}$ is defined in (3.25), $\underline{v}^{\pm}$ and $\sigma_n(\alpha)$ are given in (B.3), and n is the wedge number of $1, 2, \frac{3}{2}$, or $\frac{1}{2}$.

(ii) n = 2:

$$\bar{\bar{B}}_2 = \frac{2sin(\beta)\,\bar{\bar{I}} + \bar{\bar{\Gamma}}(\alpha_0^+)\,\bar{\bar{\Gamma}}^{-1}(-\alpha_0^-) + \bar{\bar{\Gamma}}(-\alpha_0^-)\,\bar{\bar{\Gamma}}^{-1}(\alpha_0^+)}{(2sin(\beta) + K(\alpha_0))\sigma_2(\frac{n\pi}{2} - \phi')},$$

$$\bar{\bar{D}}_2 = 2sin(\beta)\frac{\left[-2\,\bar{\bar{I}} + \bar{\bar{G}}(\alpha_0^+)\,\bar{\bar{G}}^{-1}(-\alpha_0^-) + \bar{\bar{G}}(-\alpha_0^-)\,\bar{\bar{G}}^{-1}(\alpha_0^+)\right]}{(2sin(\beta) + K(\alpha_0))}, \tag{B.6}$$

where $\alpha_0^{\pm} = \pi/2 \pm j\xi$ and ξ has the same definition as the $n = 1$ case. The matrices $\bar{\bar{G}}(\alpha)$ and $\bar{\bar{\Gamma}}(\alpha)$ are written in the following expressions:

$$\bar{\bar{G}}(\alpha) = \bar{\bar{N}}_2^{-1}(\alpha)\,\bar{\bar{Z}}_2(\alpha)\,\bar{\bar{N}}_2(\alpha),$$

$$\bar{\bar{\Gamma}}(\alpha) = \bar{\bar{N}}_2^{-1}(\alpha)\,\bar{\bar{L}}\bar{\bar{Z}}_2(\alpha)\,\bar{\bar{N}}_2(\alpha), \tag{B.7}$$

in which $\bar{\bar{N}}_2(\alpha)$ and $\bar{\bar{Z}}_2$ are the expressions given in (B.5). The function $K(\alpha_0)$ is written in terms of the functions $\tilde{M}(\alpha)$ and $\tilde{D}(\alpha, -\alpha^*)$[1], namely

$$K(\alpha_0) = 2 + \frac{4\tilde{D}(\alpha_0^+, -\alpha_0^-)\tilde{D}(-\alpha_0^+, \alpha_0^-)}{\tilde{M}(\alpha_0^+)\tilde{M}(-\alpha_0^-)}, \tag{B.8}$$

[1] "$*$" denotes complex conjugate.

in which

$$\tilde{D}(\alpha,-\alpha^*)=\Psi_h(\alpha)\Psi_e(-\alpha^*)-\Psi_e(\alpha)\Psi_h(-\alpha^*),$$

and

$$\tilde{M}(\alpha)=\Psi_e(\alpha)\Psi_h(-\alpha)+\Psi_h(\alpha)\Psi_e(-\alpha). \tag{B.9}$$

(iii) $n=\frac{3}{2}$

$$\bar{\bar{B}}_{\frac{3}{2}}=-\bar{\bar{Q}}^{-1}\bar{\bar{T}},$$

and

$$\bar{\bar{D}}_{\frac{3}{2}}=\bar{u}\underline{c}, \tag{B.10}$$

where

$$\bar{\bar{T}}=\begin{bmatrix}\underline{t}^+\\ \underline{t}^-\end{bmatrix},$$

$$\bar{\bar{Q}}=\begin{bmatrix}\underline{q}^+\\ \underline{q}^-\end{bmatrix},$$

and

$$\bar{u}=\begin{cases}\bar{u}_e, & \text{for } Z_0=\infty\\ \bar{u}_h, & \text{for } Z_0=0\end{cases}. \tag{B.11}$$

The row vectors $\underline{q}^{\pm}$ and $\underline{t}^{\pm}$ can be written as follows:

$$\begin{aligned}
\underline{q}^{\pm} &= \underline{v}^{\pm}\left\{\bar{\bar{\Psi}}\,(\alpha_0^{\pm})-\frac{\bar{\bar{\Psi}}\,(\alpha_1^{\pm})\sigma_n(\alpha_0^{\pm})\Psi_x(\alpha_0^{\pm})}{\sigma_n(\alpha_1^{\pm})\Psi_x(\alpha_1^{\pm})}\right\},\\
\underline{t}^{\pm} &= \underline{v}^{\pm}\left\{\frac{\bar{\bar{\Psi}}\,(\alpha_0^{\pm})}{\sigma_n(\alpha_0^{\pm})-\sigma_n(n\pi/2-\phi')}\right.\\
&\qquad\left.-\frac{\bar{\bar{\Psi}}\,(\alpha_1^{\pm})\sigma_n(\alpha_0^{\pm})\Psi_x(\alpha_0^{\pm})}{\left[\sigma_n(\alpha_1^{\pm})-\sigma_n(n\pi/2-\phi')\right]\sigma_n(\alpha_1^{\pm})\Psi_x(\alpha_1^{\pm})}\right\},\\
x &= \begin{cases}h, & \text{if } Z_0=0\\ e, & \text{if } Z_0=\infty\end{cases},
\end{aligned} \tag{B.12}$$

where four poles are captured within the $n\pi/2$ strips and are given as $\alpha_0^{\pm}=-\pi/4\pm j\xi$, $\alpha_1^{\pm}=3\pi/4\pm j\xi$. Moreover, the expressions for the column vectors

$\bar{u}_e$, $\bar{u}_h$ and the row vector $\underline{c}$ are given by

$$\bar{u}_e = \begin{bmatrix} 1 \\ 0 \end{bmatrix},$$

$$\bar{u}_h = \begin{bmatrix} 0 \\ 1 \end{bmatrix},$$

$$\underline{c} = \left[\frac{\underline{v}^- \bar{\bar{\Psi}}\,(\alpha_1^-)y_1}{\sigma_n(\alpha_1^-)\Psi_x(\alpha_1^-)}\right] \bar{\bar{Q}}^{-1} \bar{\bar{W}} = \left[\frac{\underline{v}^+ \bar{\bar{\Psi}}\,(\alpha_1^+)y_2}{\sigma_n(\alpha_1^+)\Psi_x(\alpha_1^+)}\right] \bar{\bar{Q}}^{-1} \bar{\bar{W}},$$

and

$$y_1 = \begin{cases} y_2 = \quad 1, & \text{if } Z_0 = 0 \\ -y_2 = \; j, & \text{if } Z_0 = \infty \end{cases} \tag{B.13}$$

where the matrix $\bar{\bar{W}}$ is given by

$$\bar{\bar{W}} = \begin{bmatrix} \underline{w}^+ \\ \underline{w}^- \end{bmatrix},$$

$$\underline{w}_\pm = \underline{v}^\pm \bar{\bar{\Psi}}\,(\alpha_0^\pm)\left\{\frac{1}{\sigma_n(\alpha_0^\pm) - \sigma_n(\frac{n\pi}{2} - \phi')} - \frac{1}{\sigma_n(\alpha_1^\pm) - \sigma_n(\frac{n\pi}{2} - \phi')}\right\}. \tag{B.14}$$

(iv) $n = \frac{1}{2}$:

$$\bar{\bar{B}}_{\frac{1}{2}} = -\bar{u}\underline{d},$$

$$\bar{\bar{D}}_{\frac{1}{2}} = \begin{bmatrix} 0 & 0 \\ 0 & 0 \end{bmatrix}, \tag{B.15}$$

in which the column vector $\bar{u}$ and the row vector $\underline{v}^+$ are given in (B.13) and (B.3), respectively. Only one pole is captured within the $n\pi/2$ strip and is given by $\alpha_1^+ = \pi/4 + j\xi$. The expression for the row vector can be written as

$$\underline{d} = \frac{\underline{v}^+ \bar{\bar{\Psi}}\,(\alpha_1^+)y_2}{\Psi_x(\alpha_1^+)\left\{\sigma_n(\alpha_1^+) - \sigma_n(n\pi/2 - \phi')\right\}}, \tag{B.16}$$

where the subscripts x and y_2 are defined in (B.12) and (B.13), respectively.

Bibliography

[1] W. D. Burnside, J. J. Kim, B. Grandchamp, R. G. Rojas, and P. Law, *Airborne Antenna Radiation Pattern Code User's Manual.* The Ohio State University, ElectroScience Laboratory, September 1985.

[2] J. J. Kim and W. D. Burnside, *Simulation and Analysis of Airborne Antenna Radiation Patterns.* Ph.D. dissertation, The Ohio State University, December 1984.

[3] J. B. Keller, "Geometrical Theory of Diffraction," *J. Opt. Soc. Am.*, vol. 52, no. 2, pp. 116–130, 1962.

[4] R. G. Kouyoumjian and P. H. Pathak, "A Uniform Geometrical Theory of Diffraction for an edge in a perfectly conducting surface," *IEEE Transactions on Antennas and Propagation*, vol. 62, pp. 1448–1461, November 1974.

[5] P. H. Pathak, N. Wang, W. D. Burnside, and R. G. Kouyoumjian, "A uniform GTD solution for the radiation from sources on a convex surface," *IEEE Transactions on Antennas and Propagation*, vol. AP-29, pp. 609–622, July 1981.

[6] J. J. Kim, N. Wang, and C. D. Chuang, "Geodesic paths of an ellipsoid-mounted antenna," tech. rep., The Ohio State University ElectroScience Laboratory, March 1982.

[7] J. J. Kim and W. D. Burnside, "Geodesic paths for side-mounted antenna on an ellipsoid model," tech. rep., The Ohio State University ElectroScience Laboratory, October 1982.

[8] M. B. Leontovich, "Investigations of Propagation of Radio Waves, Part ii," *Moscow*, 1948.

[9] G. D. Maliuzhinets, "Excitation, reflection and emission of surface waves from a wedge with given face impedances," *Soviet Phys. Dokl.*, vol. 3, pp. 752–755, 1959.

[10] R. G. Rojas, "Electromagnetic diffraction of an obliquely incident plane wave field by a wedge with impedance faces," *IEEE Transactions on Antennas and Propagation*, vol. 36, pp. 956–970, July 1988.

[11] R. G. Rojas, "Wiener-hopf analysis of the em diffraction by an impedance discontinuity in a planar surface and by an impedance half-plane," *IEEE Transactions on Antennas and Propagation*, vol. 36, pp. 71–83, January 1988.

[12] R. Rojas and H. C. Ly, "Modelling rectangular microstrip patch antennas for the airborne antenna radiation pattern code," *The Ohio State University ElectroScience Laboratory*, October 1992. personal communications.

[13] W. D. Burnside, T. H. Lee, R. Rojas, R. J. Marhefka, and D. Bensman, "Target signature modeling and bistatic scattering measurement studies," tech. rep., The Ohio State University ElectroScience Laboratory, August 1989.

[14] V. G. Vaccaro, "The generalized reflection method in electromagnetism," *Arch. Elektron Ubertragungstech*, vol. 34, pp. 493–500, 1980.

[15] V. G. Vaccaro, "Electromagnetic diffraction from a right-angled wedge with soft conditions on one face," *Optica Acta*, vol. 28, pp. 293–311, March 1981.

[16] C. Gennarelli and L. Palumbo, "A uniform asymptotic expansion of a typical diffraction integral with many coalescing simple pole singularities and a first-order saddle point," *IEEE Transactions on Antennas and Propagation*, vol. AP-32, pp. 1122–1124, October 1984.

[17] R. G. Rojas, "Comparison between two asymptotic methods," *IEEE Transactions on Antennas and Propagation*, vol. Ap-35, pp. 1489–1492, December 1987.

[18] R. G. Rojas, "Wiener-Hopf analysis of the EM diffraction by a impedance discontinuity in a planar surface and by an impedance half-plane," *IEEE Transactions on Antennas and Propagation*, vol. 36, pp. 71–83, January 1988.

[19] R. Tiberio and G. Pelosi, "High-frequency scattering from the edges of impedance discontinuities on a flat plane," *IEEE Transactions on Antennas and Propagation*, vol. Ap-31, pp. 590–596, July 1983.

[20] R. Tiberio, G. Pelosi, and G. Manara, "A uniform GTD formulation for the diffraction by a wedge with impedance faces," *IEEE Transactions on Antennas and Propagation*, vol. Ap-33, pp. 867–873, August 1985.